J. Phys. B: At. Mol. Opt. Phys. **29** (1996) 3683–3715. Printed in the UK

Excitation and ionization of neutral Cr and Mo, and the application to impurity influx

N R Badnell†, T W Gorczyca‡‖, M S Pindzola‡ and H P Summers†§

† Department of Physics and Applied Physics, University of Strathclyde, Glasgow, G4 0NG, UK
‡ Department of Physics, Auburn University, Auburn, AL, 36849, USA
§ JET Joint Undertaking, Abingdon, Oxon, OX14 3EA, UK

Received 18 December 1995, in final form 1 April 1996

Abstract. The atomic physics required to study impurity influx from a localized surface is examined and then applied to chromium and molybdenum. To this end, we have calculated term energies and oscillator strengths for the $a\ ^7\mathrm{S} \rightarrow y, z\ ^7\mathrm{P^o}$ and $a\ ^5\mathrm{S} \rightarrow y, z\ ^5\mathrm{P^o}$ transitions in neutral Cr and Mo in a multiconfiguration Hartree–Fock approximation. We have calculated excitation cross sections for these dipole transitions and for the $a\ ^7\mathrm{S} \rightarrow a\ ^5\mathrm{S}, y, z\ ^5\mathrm{P^o}$ transitions, which couple the ground to the metastable system, in a close-coupling approximation using the non-relativistic R-matrix method. Pseudo-resonances were removed from the latter transitions using a novel transformation and reduction method which eliminates those linear combinations of $(N+1)$-electron bound states that are not required by orthogonality. We have calculated the direct ionization cross sections from the ground (^{7}S) and metastable (^{5}S) terms in a distorted-wave approximation, and find significant near-threshold sensitivity to the effective potentials used. We have incorporated this primary atomic data into the Atomic Data and Analysis Structure (ADAS) and solved the quasi steady-state generalized collisional–radiative population rate equations. We present results for the number of ionization events per observed photon, the $\mathcal{SXB}$ ratio, over a wide range of electron temperatures and densities. The $\mathcal{SXB}$ ratio can be used to directly relate spectroscopic emissivity measurements to impurity flux from a localized surface such as the target plates in a magnetic fusion divertor.

1. Introduction

Heavy metal impurities are efficient radiators and, as such, are a poison to thermonuclear fusion through radiative power loss. A 10% concentration of carbon is required to quench thermonuclear fusion (at 10 keV) while a concentration of only 0.1% of molybdenum will suffice (Wesson 1987). However, the desirable engineering properties of metals means that they are ever present in fusion devices. At the Joint European Torus (JET), for example, they compose the vacuum vessel (Fe, Cr, Ni) and the radio frequency (RF) heating antennae (Cr). Consequently, low-Z materials such as beryllium and carbon are used for wall tiles and belt-limiters to limit metallic influx, and also to getter oxygen. In a material limiter plasma the last closed flux surface (LCFS) grazes the limiter and walls. Outside the LCFS the scrape-off layer (SOL), which mediates the interaction between the plasma and the walls, contains limiter impurities which also cause power loss and fuel dilution. There is also the problem of the removal of the helium 'ash' from a reactor. These impurities can be controlled through the use of a magnetic divertor. A null point in the poloidal magnetic field

‖ Present address: Department of Physics, Western Michigan University, Kalamazoo, Michigan 49008, USA.

0953-4075/96/163683+33$19.50

is created inside the LCFS. The particles in the SOL are outside of the separatrix and can be diverted onto target plates in a divertor chamber and then pumped away. The divertor plasma is both cooler and denser than the main plasma so as to reduce sputtering from the target plates and to prevent impurities entering the core plasma. The environment in the divertor chamber is quite different from that found in the edge or core plasma and different physical processes dominate. For example, molecules and molecular ions may be formed and opacity may also become a factor. There is also the question of whether a magnetic divertor is more effective in practice than a material limiter. This appears to be true for metal impurities but the case for low-Z materials (e.g. carbon) is less clear (Stangeby and McCracken 1990).

Sputtering from divertor plates provides the background for this paper, although Cr and Mo are also the subject of laser ablation studies at JET and elsewhere. The divertor plates at JET are covered with carbon or beryllium tiles, which are prone to high erosion rates. The longevity required for a machine such as the International Thermonuclear Experimental Reactor (ITER), see for example Sheffield (1994), means that studies of ways of reducing erosion rates are underway. This can be done by reducing the heat-load on the tiles by creating a 'detached' plasma or by increasing the durability of the tiles by utilizing heavy metals. A molybdenum surface is under intensive experimental investigation in Alcator C-Mod at the Massachusetts Institute of Technology and in the FTU at the Centro Ricerche Energia in Frascati, Italy. Spectroscopic determination of impurity influx from such localized surfaces is important for divertor studies so as to determine the possible leakage of impurity atoms back into the main plasma, which is highly undesirable. Behringer *et al* (1989) have considered the problem and have shown that spectroscopic measurements along a line-of-sight directed at the surface can be related to the impurity flux from the surface through the theoretical quantity the *ionizations per emitted photon* or, equivalently, its inverse—the *photon efficiency*. In the coronal approximation, the former quantity is just the ground-state ionization rate divided by the excitation rate times the radiative branching ratio from the excited state for the observed line, the so called $\mathcal{SXB}$ ratio. The plasma conditions in the divertor chamber can be far from coronal however, namely the electron density is upwards of 10^{15} cm^{-3}, the impurity atoms and ions have significant metastable populations and the time scales are such that the metastables do not have time to equilibrate. These conditions require that the atomic level populations be determined from a quasi-static generalized collisional–radiative model (see Summers and Hooper 1983). Fortunately, however, not all of the large amount of atomic data that is required for such modelling needs to be evaluated to the same degree of accuracy. Primary atomic data, namely excitation from and between metastables, ionization from metastables and oscillator strengths for the observed lines, should be calculated using state-of-the-art atomic physics codes. The remainder, secondary data, can be evaluated using a variety of simpler approaches (see Summers 1994). Behringer *et al* (1989) have carried out a detailed theoretical study related to impurity influx for a number of elements, including Cr, using only secondary data for all of the atomic processes. Also, some preliminary steps have been taken for Cr to improve on the ionization data (see Reid *et al* 1992) and excitation data (see Burke *et al* 1989), while Hibbert *et al* (1988) have carried out a detailed study of energies and oscillator strengths. The atomic data for Mo are sparse, to say the least, but studies on Cr further the way for Mo. It should be noted that the generation of reliable atomic data for species such as Cr and Mo is in itself a major undertaking. Preliminary collisional–radiative studies on light-species (Be, C) have been carried out by Dickson (1993) and it is of interest to see how the light-species behaviour contrasts with that of heavy metals.

In this paper we report on calculations of a full set of primary atomic data for both Cr and Mo. The oscillator strengths, and the structure for excitation and ionization, were calculated using the multi-configuration Hartree–Fock code (MCHF) of Froese Fischer (1991) and the AUTOSTRUCTURE code of Badnell (1986), making use of facilities not present in the original SUPERSTRUCTURE code (see Eissner *et al* 1974). The excitation cross sections were calculated in the non-relativistic close-coupling approximation using the R-matrix method (see Burke and Berrington 1993) as well as in a distorted-wave approximation. Pseudo-resonances that arose in the R-matrix exchange cross sections were eliminated using a novel transformation and reduction method due to Gorczyca *et al* (1995). The direct ionization cross sections were calculated in a distorted-wave approximation with careful attention being paid to their low-energy behaviour. To investigate the breakdown of the low-density limit, these primary atomic data were supplemented by secondary atomic data from the JET database and used in a quasi-static generalized collisional–radiative level population model, the Atomic Data and Analysis Structure (ADAS)†, see also Summers (1994), to determine $\mathcal{SXB}$ ratios over a range of divertor temperatures and densities. The role of metastable cross-coupling was also investigated. Finally, the metastable evolution during transient ionization was studied for several initial metastable fractions.

We take an integrated approach to atomic data generation and its subsequent application to plasma diagnostics. By studying the application, using state-of-the-art modelling codes, we can identify the key atomic data. Calculation of the key data using state-of-the-art atomic structure and collision codes greatly reduces the uncertainties in the accuracy of the atomic data, compared to the results of 'general formulae' that are used all too frequently. This, in turn, leads to a more rigorous testing of the plasma diagnostic. An integrated approach was the philosophy behind our earlier study on the modelling of the population structure of a carbon-seeded hydrogen plasma (see Badnell *et al* 1993a, b). Here we report on our studies of the atomic physics related to impurity influx. We do so in a single paper so as to emphasize an integrated approach. It does mean, however, that we need to discuss a number of wide-ranging topics at some depth. The layout of the paper is as follows. In section 2 we describe the theory behind the determination of impurity influx, the metastable-resolved low-density atomic model, transient ionization and metastable cross-coupling. The state-of-the-art atomic structure and collision codes, and our use of them, are detailed in section 3. The applications to Cr and Mo are described in section 4. In section 5 we present our results for the primary atomic data and for $\mathcal{SXB}$ ratios for Cr and for Mo, applicable to divertor conditions, together with predicted metastable evolution during transient ionization. We present our concluding remarks in section 6.

2. Population modelling theory

2.1. Impurity influx

We consider the situation of atoms emerging from a localized surface and being ionized successively several times. We can neglect recombination and we assume that each ionization stage is connected only with adjacent ionization stages. Using the impurity transport balance equation, Behringer *et al* (1989) have shown then that the *total* inward impurity flux Γ is related to the integral abundance for an *arbitrary* ionization stage Z

† A large amount of detailed information about ADAS is available via the World Wide Web under the URL http://patiala.phys.strath.ac.uk/adas.

along a line-of-sight directed at the surface via

$$\Gamma = \sum_{\sigma} \Gamma_{\sigma} \equiv \int_0^{\infty} N_{\rm e} \sum_{\sigma} S_{{\rm CR},\sigma}^{(z\rightarrow z+1)} N_{\sigma}^{z}(\zeta)\, {\rm d}\zeta, \tag{2.1}$$

where $N_{\rm e}$ is the electron density, $S_{{\rm CR},\sigma}^{(z\rightarrow z+1)}$ is the total effective ionization rate coefficient out of a metastable σ and $N_{\sigma}^{z}(\zeta)$ is the population number density at position ζ. The flux Γ is independent of the ionization stage Z provided no ions above stage Z emerge from the surface. In general $S_{{\rm CR},\sigma}^{(z\rightarrow z+1)}$ and $N_{\sigma}^{z}(\zeta)$ are derived using generalized collisional–radiative theory, see the appendix A to this paper for details. However, the low-density limiting case is illustrative and so it is detailed below. Note, we use the term 'metastable' state so as to denote any metastable *including* the ground state, unless specified otherwise.

2.2. Metastable-resolved low-density limit

We partition a complete set of states into metastables, denoted by σ, and excited states, denoted by i, and make the quasi-static approximation

$$\frac{{\rm d}N_{\sigma}^{z}}{{\rm d}t} \neq 0 \qquad \text{and} \qquad \frac{{\rm d}N_{i}^{z}}{{\rm d}t} = 0. \tag{2.2}$$

We assume that the excited states i are in equilibrium between excitation from a single metastable σ and radiative decay. Then

$$\sum_{k<i} A_{i\rightarrow k} N_{i}^{z} = N_{\rm e} q_{\sigma\rightarrow i} N_{\sigma}^{z}, \tag{2.3}$$

where the Einstein coefficient $A_{i\rightarrow k}$ gives the spontaneous emission rate for the $i \rightarrow k$ radiative transition and $q_{\sigma\rightarrow i}$ is the electron impact excitation rate coefficient for the $\sigma \rightarrow i$ transition, which may contain a cascade correction factor $(1 + c_{\sigma,i})$. The emissivity in the $i \rightarrow j$ line is then defined by

$$\varepsilon_{\sigma,i\rightarrow j} \equiv A_{i\rightarrow j} N_{i}^{z} = \left(\frac{A_{i\rightarrow j}}{\sum_k A_{i\rightarrow k}}\right) N_{\rm e} q_{\sigma\rightarrow i} N_{\sigma}^{z}. \tag{2.4}$$

Assuming that the plasma temperature and density are approximately constant around the position of the ionization shell of stage Z and substituting for $N_{\sigma}^{z}(\zeta)$ in equation (2.1) from (2.4), we have

$$\Gamma = \sum_{\sigma} \Gamma_{\sigma} = \sum_{\sigma} \mathcal{SXB}_{\sigma,i\rightarrow j}^{z} I_{\sigma,i\rightarrow j}, \tag{2.5}$$

where

$$I_{\sigma,i\rightarrow j} = \int_0^{\infty} \varepsilon_{\sigma,i\rightarrow j}\, {\rm d}\zeta \tag{2.6}$$

is the line-of-sight emissivity and

$$\mathcal{SXB}_{\sigma,i\rightarrow j}^{z} = \frac{S_{\sigma}^{(z\rightarrow z+1)}}{q_{\sigma\rightarrow i} A_{i\rightarrow j} / \sum_k A_{i\rightarrow k}}, \tag{2.7}$$

where

$$S_{\sigma}^{(z\rightarrow z+1)} = \sum_{\nu} S_{\nu\sigma}^{(z\rightarrow z+1)} \tag{2.8}$$

is the total zero-density ionization rate coefficient out of σ. Equation (2.5) illustrates the connection between spectroscopic measurements ($I_{\sigma,i\to j}$) and the deduced impurity flux (Γ). Its use requires the measurement of the emissivity of a line for each metastable with a significant population. The connecting $\mathcal{SXB}$ ratio denotes the number of ionizations per emitted photon and its inverse, $\mathcal{R}$, is the photon efficiency. If the excitation (and line emission) is a dipole transition then the low-density expression can hold to relatively high densities ($\sim 10^{13}$ cm^{-3}); Cr and Mo are such examples and we explore the validity of equation (2.7) in section 5. Conversely, if non-dipole excitations are dominant then several metastables can contribute significantly even at relatively low densities; the visible lines in neutral carbon are such a case, see Behringer *et al* (1989).

2.3. Transient ionization

The metastable populations satisfy

$$\frac{1}{N_e}\frac{dN_\sigma^z}{dt} = \sum_{\rho\neq\sigma}(q_{\rho\to\sigma}N_\rho^z - q_{\sigma\to\rho}N_\sigma^z) + \sum_\mu S_{\sigma\mu}^{(z-1\to z)}N_\mu^{z-1} - \sum_\nu S_{\nu\sigma}^{(z\to z+1)}N_\sigma^z. \tag{2.9}$$

For a fixed electron temperature and density the coefficients of the metastable populations in equation (2.9) are independent of time and may be solved for using an eigenvalue approach. When collisional excitation dominates over ionization the metastable populations evolve towards their equilibrium values. However, when ionization dominates (e.g. at high temperatures) each stage burns through before the metastable populations can equilibrate and they are frozen at the values at which they were born from the previous ionization stage.

2.3.1. Metastable populations. The initial metastable population distribution ($t = 0$) is not well known in general. In the absence of any measured emissivities we can only choose likely initial distributions. For example, we could take the population to be concentrated in the ground state, as is often assumed (Stangeby and McCracken 1990), or to be distributed statistically among low-lying metastables. With emissivities measured (equation (2.6)) for two or more metastables we can compare ratios of flux Γ_σ from equation (2.5) for consistency with those predicted by equation (2.1) from time-evolving our initial chosen metastable distribution. Finally, when ionization dominates, as in the case of an atom or ion emerging from a surface into a plasma, we can use the measured emissivities to reconstruct the initial metastable population distribution. We assume that the ions all move with a constant speed $v = \zeta/t$ along the ζ direction and that the temperature and density are constant. We neglect the excitation terms in (2.9) and substitute for the metastable populations using (2.4)–(2.8). On integrating from $t = 0 - \infty$ ($\zeta = 0 - \infty$) we have that

$$N_\sigma^z(t=0) = \frac{1}{v}\mathcal{SXB}_{\sigma,i\to j}^z I_{\sigma,i\to j}^z - \frac{1}{v}\sum_\mu S_{\sigma\mu}^{(z-1\to z)}\mathcal{SXB}_{\mu,k\to l}^{z-1} I_{\mu,k\to l}^{z-1}/S_\mu^{(z-1\to z)}, \tag{2.10}$$

where we have neglected $N_\sigma^z(t=\infty)$ compared to $N_\sigma^z(t=0)$ since for small Z virtually all of the population is then in the higher stages.

2.3.2. Excess energies. We assume that we have a solution for the metastable populations as a function of time t, for a given initial distribution at $t = 0$. During transient ionization,

the total radiated energy up to time t is then given by

$$\mathcal{W}_{\rm tot}(t) = \frac{N_{\rm e}}{N_{\rm tot}} \sum_{z=0}^{z=z_0} \sum_{\sigma} P_\sigma^z \int_{t'=0}^{t'=t} N_\sigma^z(t')\,{\rm d}t' \tag{2.11}$$

and the excess or deficit at time t (including $t = \infty$) compared to the equilibrium value is given by

$$\mathcal{W}_{\rm tot}^{\rm excess}(t) = \frac{N_{\rm e}}{N_{\rm tot}} \sum_{z=0}^{z=z_0} \sum_{\sigma} P_\sigma^z \int_{t'=0}^{t'=t} (N_\sigma^z(t') - N_\sigma^z(t'=\infty))\,{\rm d}t'. \tag{2.12}$$

Here Z_0 is the nuclear charge of the element and $N_{\rm tot}$ is the total elemental abundance which is constant in time. The P_σ^z term is the power loss coefficient which, in general, contains contributions from both line emission and recombination-bremsstrahlung radiation (see Summers and McWhirter 1979). The metastable-resolved line-emission contribution is given by

$$P_{{\rm L},\sigma}^z = \sum_{j,k} \frac{\Delta E_{kj} A_{j\to k} q_{\sigma\to j}}{\sum_i A_{j\to i}}, \tag{2.13}$$

still in the low-density limit.

2.4. Metastable cross-coupling

Even in the low-density limit it may be necessary to modify the approach described above by equations (2.2)–(2.4). In particular, for a sufficiently small metastable population, exchange transitions from the ground state can compete with direct excitation from a metastable as a populating mechanism for excited states, i.e. the assumption that a state i is excited from a single metastable σ (see equation (2.3)) no longer holds.

We consider the situation, still within the low-density limit of section 2.2, of a ground state plus a single metastable state that are indexed by 1 and 2 respectively. We assume that the metastable population is small compared to the population of the ground state. More precisely, we assume

$$q_{2\to 1} N_2 \ll q_{1\to 1} N_1, \tag{2.14}$$

i.e. the metastable is not a population source for states that are excited directly from the ground state, which covers most situations (population inversions excepted). We have used $q_{\sigma\to\rho}$ to denote excitation from the (ground or) metastable σ to an *excited state* i of the (ground or) metastable system indexed by ρ. Thus the population balance given by equation (2.3) remains unchanged for the ground state ($\sigma = 1$), except for the change in notation, namely

$$\sum_{k<i} A_{i\to k} N_i^z = N_{\rm e} q_{1\to 1} N_1^z. \tag{2.15}$$

However, for states excited from the metastable ($\sigma = 2$) there is an additional source term, namely

$$\sum_{l<j} A_{j\to l} N_j^z = N_{\rm e} q_{2\to 2} N_2^z + N_{\rm e} q_{1\to 2} N_1^z. \tag{2.16}$$

We assume a line-of-sight emissivity I_1 based on a particular $A_{i\to k}$ line and, similarly, an I_2 based on $A_{j\to l}$. The flux (see equation (2.1)) can then be written as

$$\Gamma = \mathcal{S}\mathcal{X}\mathcal{B}_{11} I_1 + \mathcal{S}\mathcal{X}\mathcal{B}_{22} I_2 \left(1 + \frac{N_1 q_{1\to 2}}{N_2 q_{2\to 2}}\right)^{-1} \tag{2.17}$$

or, equivalently, as

$$\Gamma = \mathcal{SXB}_{11} I_1 \left(1 - \frac{\mathcal{SXB}_{22}}{\mathcal{SXB}_{21}}\right) + \mathcal{SXB}_{22} I_2. \tag{2.18}$$

The exchange or metastable cross-coupling ratio $\mathcal{SXB}_{21}$ is given by equation (2.7).

Equation (2.17) is more suitable for studying limiting cases. For the case of a vanishingly small metastable population, and in fact more generally for

$$q_{2\to 2} N_2 \ll q_{1\to 2} N_1, \tag{2.19}$$

we have that

$$\Gamma = \mathcal{SXB}_{11} I_1, \tag{2.20}$$

as expected. Similarly, for large metastable populations, more precisely for

$$q_{2\to 2} N_2 \gg q_{1\to 2} N_1, \tag{2.21}$$

we have that

$$\Gamma = \mathcal{SXB}_{11} I_1 + \mathcal{SXB}_{22} I_2, \tag{2.22}$$

which is identical to the result that is obtained from equation (2.5), as expected.

Equation (2.18) is more informative for non-limiting cases. It is important to note that the ratio of $\mathcal{SXB}_{22}$ to $\mathcal{SXB}_{21}$ in equation (2.18) is independent of the metastable population and so that the effect of metastable cross-coupling on the particle flux depends only on the electron temperature and density and not the metastable population distribution which, at best, can be uncertain. If this ratio, $\mathcal{SXB}_{22}$ to $\mathcal{SXB}_{21}$, is sufficiently small (less than 0.2, say) over the temperature and density range of interest then metastable cross-coupling can be neglected and the result of section 2.2 (see equation (2.5) or (2.22)) can be used still. The metastable population does come into the flux determination of course through the line-of-sight emissivity I_2.

The calculated emissivity from the metastable ($\sigma = 2$) is given by (in our revised notation)

$$\varepsilon_2 = N_e N_2 \mathcal{PEC}_{22} \left(1 + \frac{q_{1\to 2} N_1}{q_{2\to 2} N_2}\right), \tag{2.23}$$

where the *photon-emissivity rate coefficient*, $\mathcal{PEC}$, is defined by

$$\mathcal{PEC}_{22} = \frac{A_{j\to l} q_{2\to 2}}{\sum_{k<j} A_{j\to k}}. \tag{2.24}$$

Assuming approximately equal total ionization rates out of the ground and metastable terms, we have that

$$\varepsilon_2 \approx N_e N_2 \mathcal{PEC}_{22} \left(1 + \frac{\mathcal{SXB}_{22} N_1}{\mathcal{SXB}_{21} N_2}\right). \tag{2.25}$$

Then, for a given ground-to-metastable population ratio, we again only require a knowledge of the ratio of $\mathcal{SXB}_{22}$ to $\mathcal{SXB}_{21}$ to tell us whether the emissivity in the metastable line is a result of direct excitation from the metastable or (exchange) excitation from the ground term.

The case of a ground state plus two or more metastables can be treated using the general formulation given in appendix A to this paper (see for example equation (A12)). Also, the restriction of equation (2.14) is no longer required by the general formulation.

3. Atomic theory

The theory of section 2 illustrates the importance of using accurate atomic data. Errors in the excitation and ionization rates translate directly into errors in the predicted impurity influx and metastable population distribution.

3.1. Atomic structure

It is still the case that the largest source of error in scattering calculations for complex atoms is due to inaccuracies in the atomic structure. We used two general codes to investigate the atomic structure of Cr and Mo, namely the MCHF code of Froese Fischer (1991) and AUTOSTRUCTURE (Badnell 1986). In the case of the MCHF code the spectroscopic radial orbitals were determined in a single configuration approximation, and pseudo-orbitals in an MCHF approximation, and then configuration-mixed to determine term energies. Oscillator strengths were evaluated by passing-on the MCHF orbital file as input to AUTOSTRUCTURE which is much more automatic in its operation. The use of AUTOSTRUCTURE, both here and for *ab initio* calculations, required changes to its operation so as to enable it to handle complex configurations. For example, the $n\,\mathrm{d}^4 n'\mathrm{p}n'\,\mathrm{d}$ configuration generates hundreds of terms and millions of Slater states and is extremely time consuming to evaluate. We recognize that for a given set of configurations we only require a subset of all of the possible $SL\pi$ terms, say $S_i L_i \pi_i$ for $i = 1, \mathrm{NAST}$. Furthermore, in LS-coupling we retain only those states $|S_i L_i \pi_i M_{S_i} M_{L_i}\rangle$ with $M_{S_i} = S_i$ and $M_{L_i} = L_i$. Through the use of the Wigner–Eckart theorem, this is sufficient for radiative transitions as well as for term energies. This specification of states greatly reduces the Slater-state expansion (see Eissner *et al* 1974). Of course, all possible Slater states that contribute to the given $M_{S_i} M_{L_i}$ are included still. This approach can be extended to intermediate coupling, provided that all significant $SL\pi$ terms are specified. Then we require all of those M_{S_i} and M_{L_i} that satisfy $M_{S_i} + M_{L_i} \geqslant |S_i - L_i|$. For Cr and Mo the code ran a thousand times faster.

A further development concerns the optimization of the radial functions. We have decoupled the specification (and operation) of the scaling parameters and the variational parameters. This greatly simplifies the use of AUTOSTRUCTURE when nl-dependent scaling and/or variational parameters are used in complex atoms. For example, Mo requires up to 15 scaling parameters but those for the valence orbitals are more important than those for the core orbitals. The nl-dependent scaling parameter approach is an independent coding (see Badnell 1988) of that due to Nussbaumer and Storey (1978) and is an integral part of the AUTOSTRUCTURE code (in fact the default) which can be used with the Thomas–Fermi–Dirac–Amaldi statistical potential or the Slater-type-orbital Hartree ($\pm$ exchange) potential. We note that the use of NAST specified terms can simplify the operation of optimization on particular terms.

3.2. Excitation

Because of the presence of pseudo-resonances, and the need for their removal, and the high partial-waves required to obtain results over a wide energy range, we make use of both close-coupling and distorted-wave methods.

3.2.1. R-matrix. We have solved the non-relativistic close-coupling equations using the R-matrix method (see Burke and Berrington 1993) to obtain collision strengths for the primary

transitions. For low partial waves ($L = 0$–8) we used the full-exchange R-matrix method in the inner region, as coded for the Opacity Project (see Berrington *et al* 1987) and for the higher partial waves ($L = 9$–80) we used the non-exchange R-matrix code (see Burke *et al* 1992). Solutions in the asymptotic region were obtained initially using the variable-phase method code VPM (see Croskery *et al* 1982) and later using the new FARM package which makes use of R-matrix propagator techniques (see Burke and Noble 1995). The collision strengths were 'topped-up' by assuming that the partial collision strengths formed a geometric series in L (see Burgess *et al* 1970). The calculated term energies were adjusted in STG3 of the R-matrix code to the $(2J + 1)$-weighted-average of the observed level energies taken from Moore (1971). Pseudo-resonances were observed in the collision strengths at higher energies due to the use of pseudo-orbitals and the over specification of the $(N + 1)$-electron expansion compared to the N-electron close-coupling expansion. Whilst (relatively) weak for the dipole transitions so that their effect could be neglected, they were prominent in the exchange transitions and accurate cross sections are required here so as to be able to determine reliably the effect of metastable cross-coupling, as described in section 2.4. The novel method, due to Gorczyca *et al* (1995), that we used to eliminate pseudo-resonances is discussed next in section 3.2.2.

In the case of Mo, the large number of bound orbitals present leads to a time-consuming evaluation of the interaction between the valence and closed-shell orbitals. Thus, we replaced the $1s^2 2s^2 2p^6 3s^2 3p^6 3d^{10} 4s^2 4p^6$ core with a model potential (see Hibbert 1989). This necessitated the use of the Iron Project (Hummer *et al* 1993) Breit–Pauli R-matrix exchange codes (see Scott and Taylor (1982) and Berrington *et al* (1995)), but run in LS coupling, since the original Opacity Project codes are not coded to handle model potentials. We also found that it was necessary to modify the interface in the non-exchange R-matrix code for model potential operation in its continuation mode (see Burke *et al* 1992). For the weaker transitions it is important to determine the valence orbitals consistently with the model potential; this point was noted by Bartschat (1993) in studies on caesium.

3.2.2. Pseudo-resonance elimination. The standard R-matrix method, like many general collision codes, uses a set of continuum basis orbitals that are orthogonal to all of the bound orbitals used in the scattering problem. The total wavefunction is expanded in terms of both target-plus-continuum basis states and equivalent coupling $(N + 1)$-electron bound states to compensate for this restriction. This is sufficient but, in general, over-sufficient compensation. The 'additional' $(N + 1)$-electron bound-state correlation can be advantageous as it improves the description of the total wavefunction when a small close-coupling expansion is used (see Burke and Taylor 1966). However, in practice one frequently encounters large 'false' or 'pseudo' resonances due to the inclusion of $(N + 1)$-electron bound states in the total wavefunction but the omission of continua, to which they are strongly coupled, from the close-coupling expansion. If all the orbitals are spectroscopic then the resonances and omitted continua are physical and the solution, in principle, is to add the missing target states to the close-coupling expansion. This can be impractical when a large configuration-interaction target expansion is used. If some of the bound orbitals are non-spectroscopic (unphysical), as they are frequently chosen to be so as to accelerate the convergence of the configuration-interaction expansion, then this approach is not realistic as the large pseudo-resonances disappear but are replaced by pseudo-Rydberg series converging to the pseudo-continua (see, for example, Berrington *et al* 1988). In principle T-matrix averaging can be used to extract the physical cross sections (see Burke *et al* 1981), but this approach does not appear to have been applied beyond neutral hydrogen

(Scholtz 1991). In practice pseudo-resonances can be eliminated approximately by forming only those $(N+1)$-electron bound states that arise from coupling a bound orbital to the set of close-coupling states, rather than the entire set of configuration-interaction states, if it is indeed possible to do so unambiguously. Failing this, pseudo-resonances are removed from the resulting cross sections simply by fitting to the cross section at energies both above and below the pseudo-resonance energy region, assuming that it is well defined.

While future developments such as *R*-matrix II (see Burke *et al* 1994, Bartschat *et al* 1996) will enable large numbers of target states to be treated, including a converged pseudo-state expansion, so as to solve the problem of pseudo-resonances, an automatic *ab initio* approach that can be implemented within the current suite of *R*-matrix codes has been developed by Gorczyca *et al* (1995). Essentially, if the presence of pseudo-resonances outweighs the value of allowing for correlation then one might as well include only those $(N+1)$-electron bound-states required by orthogonality, and no more. If the close-coupling equations are formulated using non-orthogonal continuum wavefunctions, as done originally by Percival and Seaton (1957), this is automatic. The close-coupling equations as formulated for the standard implementation of the *R*-matrix method require a little more attention, see Gorczyca *et al* (1995) for full details.

Briefly, when the close-coupling expansion is equal to the configuration-interaction target expansion then the $(N+1)$-electron bound state expansion is completely determined. When the close-coupling expansion is taken to be smaller than the configuration-interaction target expansion it may then be the case that no single choice of equivalent coupling $(N+1)$-electron bound states is physically correct. Instead, only certain linear combinations should be retained, corresponding to those required purely to compensate for the enforced orthogonality requirement. These are determined by the inequivalent couplings of the open-shell one-electron target orbitals to any target term that is included in the close coupling expansion. The transformation matrix $\mathbf{M}$ between the two $(N+1)$-electron bound-state expansions is the overlap matrix between the inequivalent-electron coupling scheme and the original equivalent-electron coupling scheme for the $(N+1)$-electron bound states. Actually the matrix $\mathbf{M}$ is not the final transformation matrix that is used because it is not generally orthonormal. Since the total wavefunction must be expanded in terms of an orthonormal basis, an orthonormal matrix $\overline{\mathbf{M}}$ is generated from $\overline{\mathbf{M}} = \mathbf{e}^{-1/2}\mathbf{O}^{\mathrm{T}}\mathbf{M}$ where $\mathbf{e}$ and $\mathbf{O}$ are the eigenvalue matrix and eigenvector matrix for the matrix $\mathbf{B} = \mathbf{M}\mathbf{M}^{\mathrm{T}}$. The eigenvalues e_i of zero-value correspond to linear combinations of the original $(N+1)$-electron bound states for which the norm of $\mathbf{O}^{\mathrm{T}}\mathbf{M}$ is zero. These linear combinations are not required in the new $(N+1)$-electron bound-state expansion. The linear combinations corresponding to an eigenvalue of $e_i = \varepsilon > 0$, but small (less than 0.1), are also omitted since they may lead to pseudo-resonances. As the eigenvalue becomes larger, it indicates that the mixing becomes stronger between the states that have been included in the close-coupling expansion and those that have been omitted and then the case becomes stronger that additional states should be included in the close-coupling expansion as well, rather than just in the configuration-interaction target expansion (assuming that they are spectroscopic). Gorczyca *et al* (1995) apply this approach to a number of cases to explore its effectiveness, including model problems where the 'exact' solution is known. The Cr/Mo problem, for which results are presented later in section 4.2, is interesting because of the strong configuration-interaction that is present between spectroscopic and pseudo-terms.

3.2.3. Distorted-wave. We have recently developed a new, general, distorted-wave program—see also Gorczyca *et al* (1994). This program, STGDW, takes continuum–

continuum collision algebra and target eigenvectors (enabling term dependence in the continuum to be taken into account) from STG2 of the R-matrix code and combines this with Slater integrals evaluated using non-orthogonal continuum distorted-wave radial functions. The use of exchange overlaps means that the continuum–bound and bound–bound $(N+1)$-electron algebra is neither required nor evaluated by STG2. This is both efficient and desirable; problems can also arise within the distorted-wave approximation if there is an imbalance between the target and configuration-interaction expansions when $(N+1)$-electron bound states are required by orthogonality. Furthermore, a partition is made between metastable states and excited states. As motivated by the population modelling theory of section 2, transitions between metastable states and excited states are of a greater priority than transitions between excited states, if we desire to reduce our computational effort. Both STG2 and STGDW evaluate only the interactions between NMETA metastable terms and NAST excited terms (which include the metastable terms). This enables us to treat a small number of metastable terms (NMETA < 10, say) and a large number of excited terms (NAST $= 1000$, say). There is no need to change to a non-exchange version of the codes for high-L since we only require the angular algebra from STG2 and exchange is automatically neglected for $L >$ LNOEX ($= 10$, by default)—then we need only evaluate the angular algebra for every-other total spin system and adjust the statistical weight accordingly in STGDW. This is all transparent to the user. The evaluation of the collision algebra by STG2 is much faster than that of many other distorted-wave codes (for example, the University College London Distorted-Wave code UCL-DW), while the partition between metastable and excited states is also highly advantageous. For large-scale problems both CPU memory and time requirements are roughly divided equally between STG2 and STGDW, assuming that the cross sections are not evaluated at more than about 10 energies—which suffices in general since there are no resonances present. Level-to-level cross sections are evaluated either through angular momentum recoupling or by term-coupling, using an independent coding of the methods detailed by Saraph (1972). The capability to treat large numbers of excited states is not needed for the Cr/Mo problem but the rapid evaluation of large numbers of partial waves is useful.

3.2.4. Reduced variables. To ensure that the collision strengths have the correct high-energy behaviour, and to present our results, we adopt the following scaling procedure suggested by Burgess and Tully (1992). We plot the reduced variables x and y, where for the *dipole transitions*

$$x = 1 - \frac{\ln C}{\ln(E_j/\Delta E_{ij} + C)} \tag{3.1}$$

and

$$y(x) = \frac{\Omega}{\ln(E_j/\Delta E_{ij} + \mathrm{e})}, \tag{3.2}$$

where E_j is the final electron energy, ΔE_{ij} is the excitation energy and C is an adjustable parameter (e is the transcendental number 2.718 2818...). Then, we have that $x = 0$ at the excitation threshold energy and $x = 1$ when $E_j = \infty$. Also, $y(0)$ equals the threshold value of the collision strength and

$$y(1) = \frac{4\omega_i f_{ij}}{\Delta E_{ij}}, \tag{3.3}$$

see Burgess and Tully (1978), where ω_i is the statistical weight of the initial state and f_{ij} the oscillator strength for the $i \to j$ transition.

For the *exchange transitions* we use

$$x = \frac{E_j}{C_2}\left(\frac{E_j}{C_2} + C_1\right)^{-1} \tag{3.4}$$

and

$$y(x) = \left(\frac{E_j}{C_2} + 1\right)^2 \Omega. \tag{3.5}$$

Badnell (1984) and Burgess and Tully (1992) have chosen $C_2 = \Delta E_{ij}$. However, this does not always result in a clear description of the high-energy behaviour of the collision strength for transitions with relatively small excitation energies, which is the case here. The infinite-energy collision strength for this transition can be determined, in principle, using the Ochkur (1964) approximation. However, the high-energy contribution to the rate coefficient is small and the high-energy results can be extrapolated readily.

3.3. Ionization

The ionization cross sections were calculated in both a configuration-average and configuration-resolved distorted-wave approximation. The configuration-average ionization (CAION) method has been described previously in the proceedings of a NATO summer school (see Pindzola *et al* 1986). The main advantage of the method is its calculational speed due to a simple final form for the angular algebra. However, the method is restricted to the single configuration approximation. The configuration-resolved ionization (CRION) method makes use of LS term-specific angular algebra, which is obtained from a modified version of Scott and Hibbert's (1982) WEIGHTS program. The method allows for the inclusion of configuration interaction in the target states and variation of the radial function for the ejected continuum with LS term (i.e. term dependence in the continuum). Two forms of the scattering may be employed in both methods. We denote the forms 'prior' and 'post' as was used by Pindzola *et al* (1995). The prior form of the scattering amplitude, see Younger (1980) and Jakubowicz and Moores (1981), requires that the incident and scattered electrons be calculated in a V_N potential while the bound and ejected electrons are calculated in a V_{N-1} potential. A post form of the scattering amplitude may also be formulated in which all electrons are calculated in a V_{N-1} potential, see Botero and Macek (1991) and Macek and Botero (1992). Although the two forms give different predictions for the cross section at the level of lowest-order perturbation theory, they should yield identical results when higher-order terms are included. Note, the order is the number of Coulomb interactions in the optical potential, the self-energy of the single-particle Green's function, when expanded by many-body diagrams (see Pan and Kelly 1990). In practice, however, it is difficult to include all higher-order terms required for the ionization of a complex atom. The prior form is physically appealing at high energies where the ejected and scattered electrons are 'slow' and 'fast' moving, respectively. The post form is physically appealing at low energies where the ejected and scattered electrons move off with similar energies. The greater sensitivity to the distorting potentials at low energies, compared to high energies, makes the post form the more physically appealing choice if one form is to be used over the entire energy range.

4. Application to Cr and Mo

We show in figure 1 a schematic diagram of the Cr/Mo system that indicates the main reaction pathways for excitation, ionization and spontaneous emission. The spacings

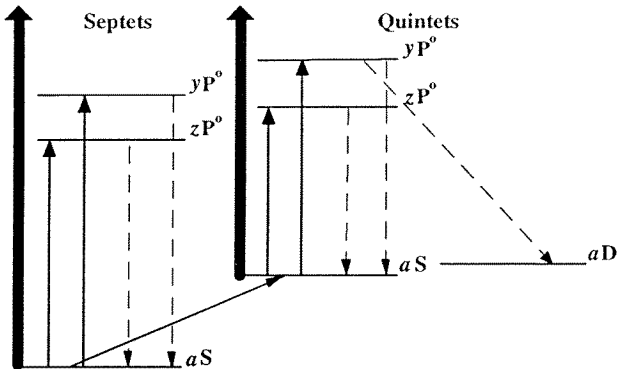

Figure 1. Main reaction pathways considered for the Cr and Mo systems. The bold full line denotes electron collisional ionization, the faint full line denotes electron collisional excitation and the broken line denotes spontaneous emission. Here $a\ ^{\omega}\mathrm{S} = n\mathrm{d}\ ^{5}(^{6}\mathrm{S})n'\mathrm{s}\ ^{\omega}\mathrm{S}$; $z\ ^{\omega}\mathrm{P^o} = n\mathrm{d}^{5}(^{6}\mathrm{S})n'\mathrm{p}\ ^{\omega}\mathrm{P^o}$; $y\ ^{\omega}\mathrm{P^o} = n\mathrm{d}^{4}n'\mathrm{s}(^{6}\mathrm{D})n'\mathrm{p}\ ^{\omega}\mathrm{P^o}$; $a\ ^{5}\mathrm{D} = n\mathrm{d}\ ^{4}n'\mathrm{s}^{2}\ ^{5}\mathrm{D}$; where $\omega = 5$ or 7, $n' = n + 1$, and $n = 3$ for Cr and $n = 4$ for Mo.

between the terms are indicative but not exact representations of the observed energy separations. Observed energy levels may be found in Moore (1971) and the $(2J + 1)$-weighted-averages are given later in tables 1 and 2. The wavelengths for the resonance lines fall in the visible range which is an important observational consideration. If we restrict ourselves to quantities (such as photon efficiencies) associated with the neutral atom, and since we neglect recombination, we do not need to follow the evolution and distribution of the ionic populations. They represent purely a loss term from the neutral species. However, the final-state resolved ionization rate coefficients are required so as to be able to follow the evolution of the neutrals through the metastable-resolved $+1$ charge state to the $+2$ charge state in our study of transient ionization.

4.1. Atomic structure

The septet and quintet structure for Cr and Mo was optimized following Hibbert *et al*'s (1988) *Calculation A* on the septet structure of Cr. For the $a\ ^{\omega}\mathrm{S}$ term ($\omega = 7$ or 5) this entailed us including the $n\mathrm{d}^{5}n'\mathrm{s}$ and $n\mathrm{d}^{4}n'\mathrm{s}n'\mathrm{d}$ configurations, where $n' = n + 1$ and $n = 3$ for Cr and $n = 4$ for Mo. For the $y, z\ ^{\omega}\mathrm{P^o}$ terms we included the $n\mathrm{d}^{5}n'\mathrm{p}, n\mathrm{d}^{4}n'\mathrm{s}n'\mathrm{p}, n\mathrm{d}^{4}n'\mathrm{s}n''\mathrm{p}, n\mathrm{d}^{4}n'\mathrm{p}n''\mathrm{s}$ and $n\mathrm{d}^{4}n'\mathrm{p}n'\mathrm{d}$ configurations, where $n'' = n' + 1$. We used the MCHF and AUTOSTRUCTURE codes rather than the CIV3 code that was used by Hibbert *et al* (1988). The $n'\mathrm{d}, n''\mathrm{s}$ and $n''\mathrm{p}$ orbitals are pseudo-orbitals optimized to compensate for the difference between the $n\mathrm{d}^{4}$ and $n\mathrm{d}^{5}$ cores which would otherwise require the use of a large spectroscopic configuration-interaction expansion. Hibbert *et al* (1988) investigated the use of more elaborate targets, this resulted in some improvement in the $a\ ^{7}\mathrm{S} \rightarrow y, z\ ^{7}\mathrm{P^o}$ energies compared with the observed (see Moore 1971), but little or no improvement in the oscillator strengths. We also require that the structure be kept to a manageable level so as to enable it to be used in subsequent collision calculations.

4.2. Excitation

Our best atomic structures were determined separately for the septet and quintet spin systems and so we carried out two separate three-state R-matrix and distorted-wave calculations for

the dipole transitions. For the exchange transitions we have to choose either the septet or quintet structure. The $a\ ^7\mathrm{S} \rightarrow a\ ^5\mathrm{S}$ collision strength was found to be relatively insensitive (5%) as to whether orbitals optimized for the septet or quintet structure were used in a two-state R-matrix calculation. However, the $y, z\ ^\omega\mathrm{P^o}$ upper states are highly mixed and sensitive to the structure that is used. Thus we used the quintet structure since we only require results for the $a\ ^7\mathrm{S} \rightarrow a\ ^5\mathrm{S}$ and $y, z\ ^5\mathrm{P^o}$ transitions. The effect of coupling on all transitions was investigated via a six-state R-matrix calculation using the quintet structure. The quintet dipole collision strengths were reduced by no more than 20% at low energies ($E < 1$ Ryd) while the $a\ ^7\mathrm{S} \rightarrow a\ ^5\mathrm{S}$ collision strength was reduced by 50% over a wide energy range. The three-state R-matrix results were used for both sets of the dipole transitions since the coupling effects from the six-state calculation are relatively small and it is debatable whether they represent any real improvement given that the 'other' spin system, and the weak resonances attached to them, is poorly described. The $a\ ^7\mathrm{S} \rightarrow a\ ^5\mathrm{S}$ and $y, z\ ^5\mathrm{P^o}$ collision strengths were taken from the six-state R-matrix results. This necessitated the removal of pseudo-resonances as discussed earlier (see section 3.2.2). The use of the quintet structure means that the resonances attached to the septet terms are of uncertain accuracy, although the term energies were adjusted to the observed ones in both the R-matrix and distorted-wave calculations, of course. This uncertainty for the exchange transitions has its greatest effect at low energies and temperatures. However, the $a\ ^7\mathrm{S} \rightarrow a\ ^5\mathrm{S}$ collision strength is only required for the evolution of the metastables, and the $a\ ^7\mathrm{S} \rightarrow y, z\ ^5\mathrm{P^o}$ collision strengths only have a secondary effect on the deduction of impurity influx (see section 2.4).

Finally, the radius of the R-matrix box was 29.0 au for Cr and 29.2 au for Mo, and we used 50 continuum basis orbitals. Both the R-matrix and distorted-wave calculations used partial waves up to $L = 80$ before being 'topped-up' and the highest collision energy that we used was 15 Ryd.

4.3. Ionization

The CAION code was employed to calculate total and differential ionization cross sections for the $n\mathrm{d}^5 n'\mathrm{s}n\mathrm{d}^5$ and $n\mathrm{d}^5 4\mathrm{s} \rightarrow n\mathrm{d}^4 n'\mathrm{s}$ transitions in Cr ($n = 3, n' = 4$) and Mo ($n = 4, n' = 5$). The CRION code was employed to calculate the total and differential ionization cross sections for the ground $n\mathrm{d}^5(^6\mathrm{S})n'\mathrm{s}\ ^7\mathrm{S} \rightarrow n\mathrm{d}^5\ ^6\mathrm{S}$ and $n\mathrm{d}^5(^6\mathrm{S})n'\mathrm{s}\ ^7\mathrm{S} \rightarrow n\mathrm{d}^4(^5\mathrm{D})n'\mathrm{s}\ ^6\mathrm{D}$ transitions as well as for the metastable $n\mathrm{d}^5(^6\mathrm{S})n'\mathrm{s}\ ^5\mathrm{S} \rightarrow n\mathrm{d}^5\ ^6\mathrm{S}$ and the $n\mathrm{d}^5(^6\mathrm{S})n'\mathrm{s}\ ^5\mathrm{S} \rightarrow n\mathrm{d}^4(^5\mathrm{D})n'\mathrm{s}\ ^\omega\mathrm{D}$ transitions for $\omega = 4$ and 6. The CRION calculations used the experimental ionization energies given in Moore's (1971) tables. The LS term-specific ionization cross sections are equal to their configuration-average ionization cross sections except for the metastable $n\mathrm{d}^5(^6\mathrm{S})n'\mathrm{s}\ ^5\mathrm{S} \rightarrow n\mathrm{d}^4\ (^5\mathrm{D})n'\mathrm{s}\ ^\omega\mathrm{D}$ transitions which are equal to 24/25 and 1/25 of the cross section for the $n\mathrm{d}^5 n'\mathrm{s} \rightarrow n\mathrm{d}^4 n'\mathrm{s}$ transition, for $\omega = 4$ and 6, respectively.

5. Results

5.1. Atomic structure

We present our results for the term energies and oscillator strengths for the septet and quintet spin systems in Cr and Mo in tables 1 and 2, respectively, and compare them with the results of Hibbert *et al* (1988) and experiment, where possible. Overall, there is a similar level of agreement between the MCHF and CIV3 results and with experiment. This is not too surprising since the calculations are of a similar nature, but they do give us a guide as to

Table 1. Energies (Ryd) and oscillator strengths for septet and quintet terms in Cr.

	$a\ ^7\mathrm{S} \rightarrow z\ ^7\mathrm{P^o}$	$a\ ^7\mathrm{S} \rightarrow y\ ^7\mathrm{P^o}$	$a\ ^5\mathrm{S} \rightarrow z\ ^5\mathrm{P^o}$	$a\ ^5\mathrm{S} \rightarrow y\ ^5\mathrm{P^o}$
ΔE(obs)[a]	0.213	0.254	0.175	0.201
gf(exp)[b]	1.79	5.99–6.19	—	—
ΔE(MCHF)[c]	0.195	0.236	0.136	0.201
gf(MCHF)	2.03	6.02	4.23	0.19
ΔE(CIV3)[d]	0.188	0.236	0.168	0.204
gf(CIV3)	1.65	7.92	3.42	0.44
ΔE(AS)[e]	0.182	0.204	0.126	0.153
gf(AS)	2.24	5.11	3.77	0.21

[a] Moore (1971).
[b] Huber and Sanderman (1977) and Blackwell *et al* (1984).
[c] This work, using MCHF.
[d] Hibbert *et al* (1988).
[e] This work, using AUTOSTRUCTURE.

Table 2. Energies (Ryd) and oscillator strengths for septet and quintet terms in Mo.

	$a\ ^7\mathrm{S} \rightarrow z\ ^7\mathrm{P^o}$	$a\ ^7\mathrm{S} \rightarrow y\ ^7\mathrm{P^o}$	$a\ ^5\mathrm{S} \rightarrow z\ ^5\mathrm{P^o}$	$a\ ^5\mathrm{S} \rightarrow y\ ^5\mathrm{P^o}$
ΔE(obs)[a]	0.237	0.287	0.165	0.207
gf(exp)	—	—	—	—
ΔE(MCHF)[b]	0.194	0.283	0.118	0.227
gf(MCHF)	5.12	5.71	4.10	0.28
ΔE(AS)[c]	0.183	0.371	0.118	0.291
gf(AS)	6.54	3.65	4.00	0.10

[a] Moore (1971).
[b] This work, using MCHF.
[c] This work, using AUTOSTRUCTURE.

uncertainties. The AUTOSTRUCTURE results are slightly worse overall and so we use our MCHF structures in all of our collision calculations. For Mo there is much better agreement between the MCHF and AUTOSTRUCTURE results for the $a\ ^{\omega}\mathrm{S} \rightarrow z\ ^{\omega}\mathrm{P^o}$ transition (both septet and quintet) than for the $a\ ^{\omega}\mathrm{S} \rightarrow y\ ^{\omega}\mathrm{P^o}$. This indicates that the $a\ ^{\omega}\mathrm{S} \rightarrow z\ ^{\omega}\mathrm{P^o}$ transition is the more reliable line to measure for the emissivity. Also, for the quintet spin system, radiative transitions from the $z\ ^5\mathrm{P^o}$ are unaffected by branching, unlike those from the $y\ ^5\mathrm{P^o}$.

5.2. Excitation

We present our R-matrix and distorted-wave results for the excitation of Cr and Mo in figures 2(a)–(g) and 3(a)–(g), calculated according to sections 3.2.1 and 3.2.3. The septet dipole transitions, see figures 2(a), (b) and 3(a), (b), are shown converging to their infinite energy limit (see section 3.2.4). The quintet dipole transitions, see figures 2(c), (d) and 3(c), (d), converge to their infinite-energy limit more slowly than the septet transitions do and extrapolation would be subject to a much larger uncertainty and/or error without the limit point ($X = 1$). The highest calculated energy (15 Ryd) corresponds to about $X = 0.65$ in our scaled energy units for the dipole transitions. Our distorted-wave results overestimate the dipole collision strengths by up to a factor of two at 0.5 Ryd, but by 1 Ryd the overestimate has fallen to at most 20%. As the incident energy is increased

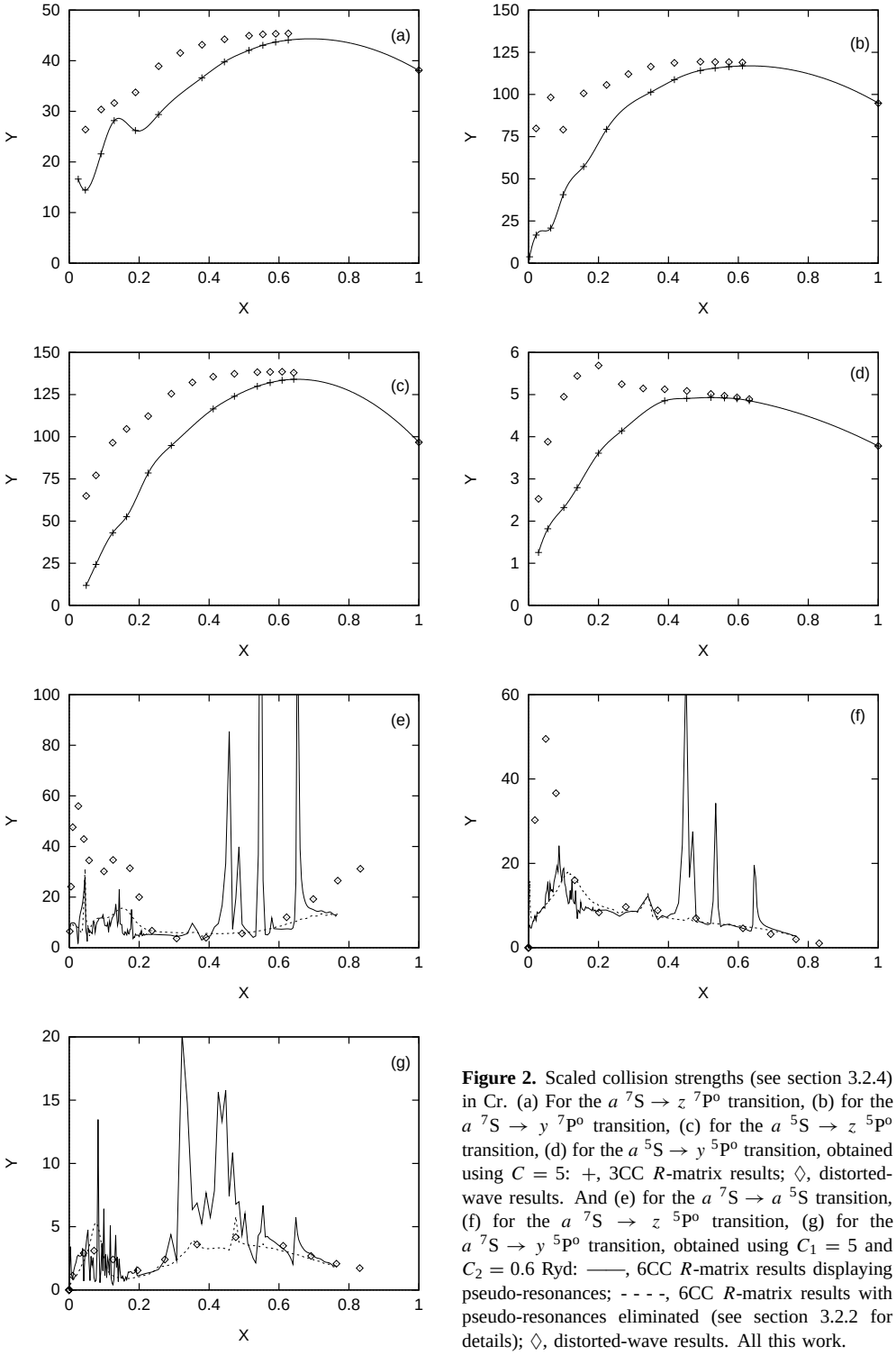

Figure 2. Scaled collision strengths (see section 3.2.4) in Cr. (a) For the $a\ ^7\mathrm{S} \rightarrow z\ ^7\mathrm{P^o}$ transition, (b) for the $a\ ^7\mathrm{S} \rightarrow y\ ^7\mathrm{P^o}$ transition, (c) for the $a\ ^5\mathrm{S} \rightarrow z\ ^5\mathrm{P^o}$ transition, (d) for the $a\ ^5\mathrm{S} \rightarrow y\ ^5\mathrm{P^o}$ transition, obtained using $C = 5$: +, 3CC R-matrix results; ◊, distorted-wave results. And (e) for the $a\ ^7\mathrm{S} \rightarrow a\ ^5\mathrm{S}$ transition, (f) for the $a\ ^7\mathrm{S} \rightarrow z\ ^5\mathrm{P^o}$ transition, (g) for the $a\ ^7\mathrm{S} \rightarrow y\ ^5\mathrm{P^o}$ transition, obtained using $C_1 = 5$ and $C_2 = 0.6$ Ryd: ——, 6CC R-matrix results displaying pseudo-resonances; - - - -, 6CC R-matrix results with pseudo-resonances eliminated (see section 3.2.2 for details); ◊, distorted-wave results. All this work.

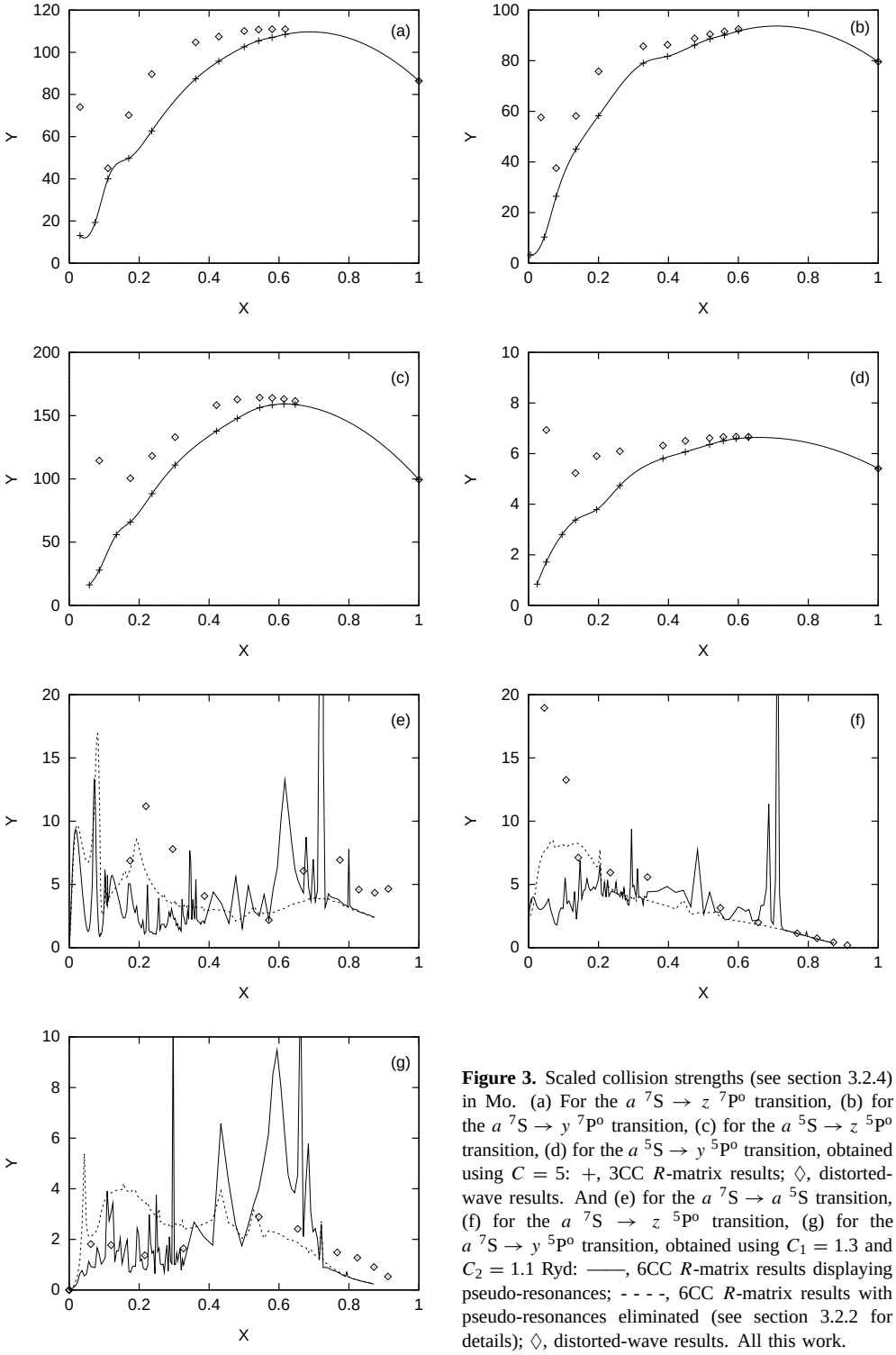

Figure 3. Scaled collision strengths (see section 3.2.4) in Mo. (a) For the $a\ ^7\mathrm{S} \rightarrow z\ ^7\mathrm{P^o}$ transition, (b) for the $a\ ^7\mathrm{S} \rightarrow y\ ^7\mathrm{P^o}$ transition, (c) for the $a\ ^5\mathrm{S} \rightarrow z\ ^5\mathrm{P^o}$ transition, (d) for the $a\ ^5\mathrm{S} \rightarrow y\ ^5\mathrm{P^o}$ transition, obtained using $C = 5$: +, 3CC R-matrix results; ◊, distorted-wave results. And (e) for the $a\ ^7\mathrm{S} \rightarrow a\ ^5\mathrm{S}$ transition, (f) for the $a\ ^7\mathrm{S} \rightarrow z\ ^5\mathrm{P^o}$ transition, (g) for the $a\ ^7\mathrm{S} \rightarrow y\ ^5\mathrm{P^o}$ transition, obtained using $C_1 = 1.3$ and $C_2 = 1.1$ Ryd: ——, 6CC R-matrix results displaying pseudo-resonances; - - - -, 6CC R-matrix results with pseudo-resonances eliminated (see section 3.2.2 for details); ◊, distorted-wave results. All this work.

further, our R-matrix and distorted-wave results converge ever closer. No attempt was made to resolve the relatively weak resonance structure in the $a\ ^{\omega}\mathrm{S} \rightarrow z\ ^{\omega}\mathrm{P^o}$ transition below the $y\ ^{\omega}\mathrm{P^o}$ threshold, only the background collision strength was used. This is the reason for the results starting just above $X = 0$ in the plots. The excitation thresholds are at $X = 0$, for which $Y = 0$ for neutrals, of course. Our dipole results for Cr are in broad agreement with the preliminary estimates made by Burke *et al* (1989), when we make approximations similar to those that they had to make to render the problem tractable at the time.

For the exchange transitions, see figures 2(e)–(g) and 3(e)–(g), our distorted-wave results overestimate the collision strengths substantially at low energies compared to our six-state R-matrix results but converge well to them at higher energies. Our six-state R-matrix results exhibit large pseudo-resonances over a wide energy range. Also shown are our six-state R-matrix results with the pseudo-resonances eliminated according to the procedure described in section 3.2.2. The results for Cr following pseudo-resonance elimination, see figure 2(e)–(g), are what one might expect intuitively, they track the background of the pseudo-resonant results. For the case of Mo, see figure 3(e)–(g), the results with the pseudo-resonances eliminated are somewhat larger than the original results at low energies ($X < 0.2$). This increase may well be due to the fact that our pseudo-resonance elimination procedure results in a *reduction* of the number of $(N + 1)$-electron bound states. Past experience has shown that *increasing* the number of $(N + 1)$-electron bound states, so as to allow for correlation, often results in a reduction of the collision strength. We also note that we obtained several large eigenvalues (around 0.1) from our transformation matrix (actually $\mathbf{B} = \mathbf{M}\mathbf{M}^{\mathrm{T}}$ of course) and that our spectroscopic and pseudo-terms are highly-mixed. As discussed in section 3.2.2 this indicates that it may be necessary to use spectroscopic nl-orbitals instead of pseudo-orbitals for nl and then use pseudo-$(n + 1)l$ orbitals to obtain more accurate results. For the purposes of our application, the existing results are sufficiently accurate for now. Finally, for the $a\ ^7\mathrm{S} \rightarrow a\ ^5\mathrm{S}$ transition but not the $a\ ^7\mathrm{S} \rightarrow y, z\ ^5\mathrm{P^o}$ transitions, there is some evidence that the *scaled* distorted-wave and six-state R-matrix collision strengths start to separate at the highest energies, $X > 0.8$ (15 Ryd), but this is not apparent with the two-state R-matrix results for this transition (not shown). This separation may be the result of a weak coupling to the $^7\mathrm{P^o}$ terms, which are dipole excited; the exchange collision strengths fall-off much more rapidly with energy than the dipole collision strengths, and so weak coupling effects may manifest themselves at high energies. However, the unscaled collision strengths from all of the methods are small and rapidly decreasing here at $X > 0.8$ (15 Ryd).

5.3. Ionization

We present our near threshold ionization cross section results for selected transitions in Cr and Mo in figures 4(a)–(e) and 5(a)–(e), respectively. The prior form scattering amplitude results are given by the broken curves, *all* of which exhibit a giant shape resonance. The post form scattering amplitude results are given by the full curves, all of which are devoid of shape-resonance features. The resonance is more noticeable for those ionizing transitions which leave the ion in an excited state (see figures 4(c)–(e) and 5(c)–(e)) rather than in the ground state (see figures 4(a), (b) and 5(a), (b)). The resonance is found in the d-wave channel of the scattered wavefunction calculated in a V_N potential of the neutral atom. The giant shape resonance is most clearly observed in the ionization cross section that is differential with ejected energy where a typical

Table 3. (*a*) Direct $\mathcal{SXB}_{77}$ ratio (ionizations/photon) for Cr $z\ ^7P^o \rightarrow a\ ^7S$ ($\lambda = 4270.7$ Å). (*b*) Direct $\mathcal{SXB}_{77}$ ratio (ionizations/photon) for Cr $y\ ^7P^o \rightarrow a\ ^7S$ ($\lambda = 3590.9$ Å). (*c*) Direct $\mathcal{SXB}_{55}$ ratio (ionizations/photon) for Cr $z\ ^5P^o \rightarrow a\ ^5S$ ($\lambda = 5208.3$ Å). (*d*) Direct $\mathcal{SXB}_{55}$ ratio (ionizations/photon) for Cr $y\ ^5P^o \rightarrow a\ ^5S$ ($\lambda = 4530.9$ Å). (*e*) Exchange $\mathcal{SXB}_{57}$ ratio (ionizations/photon) for Cr $z\ ^5P^o \rightarrow a\ ^5S$ ($\lambda = 5208.3$ Å). (*f*) Exchange $\mathcal{SXB}_{57}$ ratio (ionizations/photon) for Cr $y\ ^5P^o \rightarrow a\ ^5S$ ($\lambda = 4530.9$ Å).

	Electron density (cm^{-3})						
T_e (eV)	1.00^{12}	1.00^{13}	1.00^{14}	5.00^{14}	1.00^{15}	2.00^{15}	5.00^{15}
(*a*)							
1.0	$7.33^{-3\dagger}$	8.42^{-3}	1.87^{-2}	6.63^{-2}	1.29^{-1}	2.59^{-1}	6.55^{-1}
2.0	7.99^{-2}	9.00^{-2}	1.83^{-1}	6.08^{-1}	1.16	2.30	5.74
5.0	4.07^{-1}	4.50^{-1}	8.72^{-1}	2.86	5.46	1.07^{1}	2.67^{1}
10.0	7.48^{-1}	8.27^{-1}	1.62	5.43	1.04^{1}	2.05^{1}	5.10^{1}
20.0	1.03	1.14	2.26	7.71	1.48^{1}	2.93^{1}	7.31^{1}
50.0	1.30	1.43	2.75	9.24	1.78^{1}	3.52^{1}	8.79^{1}
100.0	1.42	1.56	2.87	9.29	1.04^{1}	3.51^{1}	8.78^{1}
(*b*)							
1.0	1.15^{-2}	1.27^{-2}	2.15^{-2}	4.57^{-2}	7.12^{-2}	1.20^{-1}	2.63^{-1}
2.0	7.57^{-2}	8.25^{-2}	1.13^{-1}	2.78^{-1}	4.43^{-1}	7.63^{-1}	1.72
5.0	2.35^{-1}	2.52^{-1}	3.89^{-1}	8.78^{-1}	1.45	2.59	5.99
10.0	3.46^{-1}	3.70^{-1}	5.72^{-1}	1.34	2.25	4.07	9.50
20.0	4.29^{-1}	4.58^{-1}	7.07^{-1}	1.67	2.82	5.10	1.19^{1}
50.0	5.09^{-1}	5.40^{-1}	8.11^{-1}	1.86	3.11	5.60	1.30^{1}
100.0	5.55^{-1}	5.88^{-1}	8.49^{-1}	1.86	3.07	5.48	1.26^{1}
(*c*)							
1.0	7.26^{-3}	8.59^{-3}	2.02^{-2}	6.75^{-2}	1.26^{-1}	2.42^{-1}	5.91^{-1}
2.0	3.79^{-2}	4.60^{-2}	1.16^{-1}	4.05^{-1}	7.62^{-1}	1.48	3.62
5.0	1.13^{-1}	1.39^{-1}	3.58^{-1}	1.28	2.43	4.73	1.16^{1}
10.0	1.79^{-1}	2.21^{-1}	5.66^{-1}	2.04	3.89	7.58	1.86^{1}
20.0	2.39^{-1}	2.91^{-1}	7.34^{-1}	2.64	5.03	9.80	2.41^{1}
50.0	3.01^{-1}	3.59^{-1}	8.56^{-1}	3.01	5.70	1.11^{1}	2.72^{1}
100.0	3.34^{-1}	3.91^{-1}	8.74^{-1}	3.00	5.65	1.09^{1}	2.68^{1}
(*d*)							
1.0	1.24^{-1}	1.53^{-1}	2.88^{-1}	4.58^{-1}	8.01^{-1}	1.84	3.56
2.0	7.14^{-1}	9.41^{-1}	1.98	3.30	5.99	1.41^{1}	2.78^{1}
5.0	2.53	3.75	9.60	1.74^{1}	3.34^{1}	8.25^{1}	1.65^{2}
10.0	4.38	7.00	1.99^{1}	3.75^{1}	7.43^{1}	1.88^{2}	3.78^{2}
20.0	6.25	1.04^{1}	3.10^{1}	5.94^{1}	1.19^{2}	3.04^{2}	6.16^{2}
50.0	8.41	1.38^{1}	4.04^{1}	7.70^{1}	1.54^{2}	3.92^{2}	7.94^{2}
100.0	9.70	1.53^{1}	4.24^{1}	7.90^{1}	1.55^{2}	3.90^{2}	7.89^{2}
(*e*)							
1.0	3.86^{-2}	4.39^{-2}	9.26^{-2}	3.22^{-1}	6.49^{-1}	1.37	3.68
2.0	4.24^{-1}	4.75^{-1}	9.65^{-1}	3.51	7.24	1.55^{1}	4.17^{1}
5.0	3.23	3.60	7.55	2.94^{1}	6.08^{1}	1.28^{2}	3.36^{2}
10.0	1.06^{1}	1.18^{1}	2.57^{1}	1.02^{2}	2.10^{2}	4.35^{2}	1.12^{3}
20.0	3.05^{1}	3.42^{1}	7.51^{1}	2.98^{2}	6.07^{2}	1.25^{3}	3.20^{3}
50.0	1.14^{2}	1.26^{2}	2.68^{2}	1.03^{3}	2.07^{3}	4.23^{3}	1.08^{4}
100.0	2.76^{2}	2.95^{2}	6.11^{2}	2.22^{3}	4.53^{3}	9.03^{3}	2.37^{4}
(*f*)							
1.0	2.97^{-1}	3.65^{-1}	6.94^{-1}	1.15	2.17	5.74	1.26^{1}
2.0	2.40	3.04	6.23	1.08^{1}	2.14^{1}	5.98^{1}	1.36^{2}
5.0	1.74^{1}	2.43^{1}	5.93^{1}	1.12^{2}	2.32^{2}	6.76^{2}	1.53^{3}
10.0	5.78^{1}	8.67^{1}	2.35^{2}	4.55^{2}	9.69^{2}	2.82^{3}	6.30^{3}
20.0	1.63^{2}	2.54^{2}	7.24^{2}	1.42^{3}	3.03^{3}	8.76^{3}	1.94^{4}
50.0	5.60^{2}	8.75^{2}	2.47^{3}	4.80^{3}	1.02^{4}	2.90^{4}	6.36^{4}
100.0	1.27^{3}	1.94^{3}	5.24^{3}	1.12^{4}	2.14^{4}	5.92^{4}	1.23^{5}

$^{\dagger}7.33^{-3}$ denotes 7.33×10^{-3}.

Table 4. (*a*) Direct $\mathcal{SX}\mathcal{B}_{77}$ ratio (ionizations/photon) for Mo $z\ ^7\mathrm{P^o} \rightarrow a\ ^7\mathrm{S}$ ($\lambda = 3845.7$ Å). (*b*) Direct $\mathcal{SX}\mathcal{B}_{77}$ ratio (ionizations/photon) for Mo $y\ ^7\mathrm{P^o} \rightarrow a\ ^7\mathrm{S}$ ($\lambda = 3160.5$ Å). (*c*) Direct $\mathcal{SX}\mathcal{B}_{55}$ ratio (ionizations/photon) for Mo $z\ ^5\mathrm{P^o} \rightarrow a\ ^5\mathrm{S}$ ($\lambda = 5229.5$ Å). (*d*) Direct $\mathcal{SX}\mathcal{B}_{55}$ ratio (ionizations/photon) for Mo $y\ ^5\mathrm{P^o} \rightarrow a\ ^7\mathrm{S}$ ($\lambda = 4394.3$ Å). (*e*) Exchange $\mathcal{SX}\mathcal{B}_{57}$ ratio (ionizations/photon) for Mo $z\ ^5\mathrm{P^o} \rightarrow a\ ^5\mathrm{S}$ ($\lambda = 5529.5$ Å). (*f*) Exchange $\mathcal{SX}\mathcal{B}_{57}$ ratio (ionizations/photon) for Mo $y\ ^5\mathrm{P^o} \rightarrow a\ ^5\mathrm{S}$ ($\lambda = 4394.3$ Å).

	Electron density (cm^{-3})						
T_e (eV)	1.00^{12}	1.00^{13}	1.00^{14}	5.00^{14}	1.00^{15}	2.00^{15}	5.00^{15}
(*a*)							
1.0	7.41^{-3}	7.88^{-3}	1.20^{-2}	2.68^{-2}	4.40^{-2}	7.86^{-2}	1.86^{-1}
2.0	7.43^{-2}	7.79^{-2}	1.09^{-1}	2.32^{-1}	3.83^{-1}	6.92^{-1}	1.64
5.0	3.35^{-1}	3.49^{-1}	4.75^{-1}	1.03	1.73	3.17	7.51
10.0	6.04^{-1}	6.28^{-1}	8.59^{-1}	1.90	3.24	5.95	1.41^{1}
20.0	8.72^{-1}	9.05^{-1}	1.24	2.74	4.67	8.57	2.03^{1}
50.0	1.19	1.23	1.64	3.53	5.93	1.08^{1}	2.54^{1}
100.0	1.39	1.43	1.87	3.80	6.31	1.11^{1}	2.64^{1}
	Electron density (cm^{-3})						
T_e (eV)	1.00^{13}	1.00^{14}	5.00^{14}	1.00^{15}	2.00^{15}	5.00^{15}	1.00^{16}
(*b*)							
1.0	2.31^{-2}	3.38^{-2}	6.54^{-2}	9.54^{-2}	1.48^{-1}	2.95^{-1}	5.34^{-1}
2.0	1.41^{-1}	1.89^{-1}	3.50^{-1}	5.26^{-1}	8.57^{-1}	1.82	3.42
5.0	4.61^{-1}	5.99^{-1}	1.14	1.78	3.04	6.77	1.30^{1}
10.0	7.69^{-1}	9.94^{-1}	1.92	3.04	5.26	1.19^{1}	2.28^{1}
20.0	1.10	1.41	2.70	4.27	7.38	1.66^{1}	3.21^{1}
50.0	1.52	1.90	3.49	5.42	9.25	2.07^{1}	3.97^{1}
100.0	1.79	2.19	3.84	5.82	9.79	2.13^{1}	4.11^{1}
	Electron density (cm^{-3})						
T_e (eV)	1.00^{12}	1.00^{13}	1.00^{14}	5.00^{14}	1.00^{15}	2.00^{15}	5.00^{15}
(*c*)							
1.0	9.85^{-3}	1.06^{-2}	1.91^{-2}	6.14^{-2}	1.15^{-1}	2.23^{-1}	5.45^{-1}
2.0	4.69^{-2}	5.19^{-2}	1.12^{-1}	3.99^{-1}	7.60^{-1}	1.48	3.65
5.0	1.45^{-1}	1.65^{-1}	3.91^{-1}	1.43	2.73	5.34	1.32^{1}
10.0	2.43^{-1}	2.79^{-1}	6.66^{-1}	2.42	4.62	9.01	2.22^{1}
20.0	3.55^{-1}	4.05^{-1}	9.36^{-1}	3.33	6.31	1.23^{1}	3.02^{1}
50.0	5.04^{-1}	5.67^{-1}	1.22	4.17	7.86	1.52^{1}	3.74^{1}
100.0	5.99^{-1}	6.68^{-1}	1.34	4.50	8.41	1.62^{1}	3.97^{1}
	Electron density (cm^{-3})						
T_e (eV)	1.00^{11}	1.00^{12}	1.00^{13}	1.00^{14}	2.00^{14}	5.00^{14}	1.00^{15}
(*d*)							
1.0	1.16	1.10	7.74^{-1}	5.63^{-1}	7.20^{-1}	1.30	2.30
2.0	4.71	4.37	2.88	2.62	3.72	7.30	1.34^{1}
5.0	1.48^{1}	1.34^{1}	8.48	9.54	1.43^{1}	2.95^{1}	5.49^{1}
10.0	2.61^{1}	2.36^{1}	1.50^{1}	1.82^{1}	2.77^{1}	5.75^{1}	1.07^{2}
20.0	3.92^{1}	3.56^{1}	2.34^{1}	2.88^{1}	4.36^{1}	8.99^{1}	1.68^{2}
50.0	5.67^{1}	5.16^{1}	3.37^{1}	3.88^{1}	5.76^{1}	1.16^{2}	2.15^{2}
100.0	6.83^{1}	6.13^{1}	3.71^{1}	3.88^{1}	5.62^{1}	1.12^{2}	2.04^{2}

Table 4. (Continued)

	Electron density (cm^{-3})						
T_e (eV)	1.00^{12}	1.00^{13}	1.00^{14}	5.00^{14}	1.00^{15}	2.00^{15}	5.00^{15}
(*e*)							
1.0	3.00^{-2}	3.24^{-2}	5.63^{-2}	1.86^{-1}	3.90^{-1}	8.86^{-1}	2.68
2.0	4.75^{-1}	5.04^{-1}	8.27^{-1}	2.71	5.70	1.27^{1}	3.67^{1}
5.0	5.33	5.62	9.57	3.36^{1}	6.99^{1}	1.50^{2}	4.05^{2}
10.0	2.19^{1}	2.31^{1}	4.11^{1}	1.48^{2}	3.02^{2}	6.33^{2}	1.663
20.0	7.56^{1}	7.99^{1}	1.44^{2}	5.12^{2}	1.03^{3}	2.12^{3}	5.48^{3}
50.0	3.34^{2}	3.50^{2}	6.11^{2}	2.07^{3}	4.08^{3}	8.29^{3}	2.12^{4}
100.0	8.63^{2}	8.96^{2}	1.49^{3}	4.90^{3}	9.42^{3}	1.90^{4}	4.82^{4}

	Electron density (cm^{-3})						
T_e (eV)	1.00^{11}	1.00^{12}	1.00^{13}	1.00^{14}	2.00^{14}	5.00^{14}	1.00^{15}
(*f*)							
1.0	2.94^{-1}	2.97^{-1}	3.32^{-1}	6.79^{-1}	1.09	2.51	5.40
2.0	2.51	2.55	2.97	6.96	1.16^{1}	2.81^{1}	6.17^{1}
5.0	1.75^{1}	1.80^{1}	2.26^{1}	6.67^{1}	1.20^{2}	3.05^{2}	6.67^{2}
10.0	5.74^{1}	5.92^{1}	7.74^{1}	2.58^{2}	4.77^{2}	1.23^{3}	2.65^{3}
20.0	1.71^{2}	1.77^{2}	2.35^{2}	8.25^{2}	1.54^{3}	3.94^{3}	8.37^{3}
50.0	6.72^{2}	6.96^{2}	9.52^{2}	3.20^{3}	5.88^{3}	1.47^{4}	3.08^{4}
100.0	1.47^{3}	1.72^{3}	2.32^{3}	7.62^{3}	1.38^{4}	3.37^{4}	6.94^{4}

resonance profile is obtained. Recent calculations for the direct ionization cross section of neutral Cu and Fe show a similar large discrepancy between the post and prior forms due to the appearance of a giant resonance, see Griffin and Pindzola (1995) and Pindzola *et al* (1995). The experiments on Cu and Fe by Freund *et al* (1990) clearly favour the post form results and the absence of a giant resonance. Furthermore, recent distorted-wave and time-dependent close-coupling calculations by Pindzola and Schultz (1996) and Pindzola and Robicheaux (1996) for the ionization of hydrogen show that the post form is the best choice for low partial waves (and that the prior form is the best choice for high partial waves). Since the shape resonance is in the d-wave of the prior form results, the results of the post form are the better choice of the two limited methods for Cr and Mo. Thus we use the results of the post approximation in our solution of the collisional–radiative equations. Our post form distorted-wave results for the ground state $3d^5(^6S)4s\ ^7S \rightarrow 3d^5\ ^6S$ and $3d^5(^6S)4s\ ^7S \rightarrow 3d^4\ (^5D)4s\ ^6D$ transitions in Cr are in reasonable agreement with the previous distorted-wave/*R*-matrix hybrid results of Reid *et al* (1992) in the near-threshold energy region. Even though the distorted-wave/*R*-matrix calculations make use of the prior form of the scattering amplitude, exchange is neglected in the potentials for the incident and scattered wavefunctions. We find that such an omission results in the shape resonance disappearing from our prior form distorted-wave results. Our distorted-wave results do not include excitation–autoionization contributions, which are usually relatively small for neutral atoms, but are included in the distorted-wave/*R*-matrix results. Further CRION calculations on Cr have shown that the ionization cross sections are somewhat sensitive to polarization effects, which are not included in either set of results.

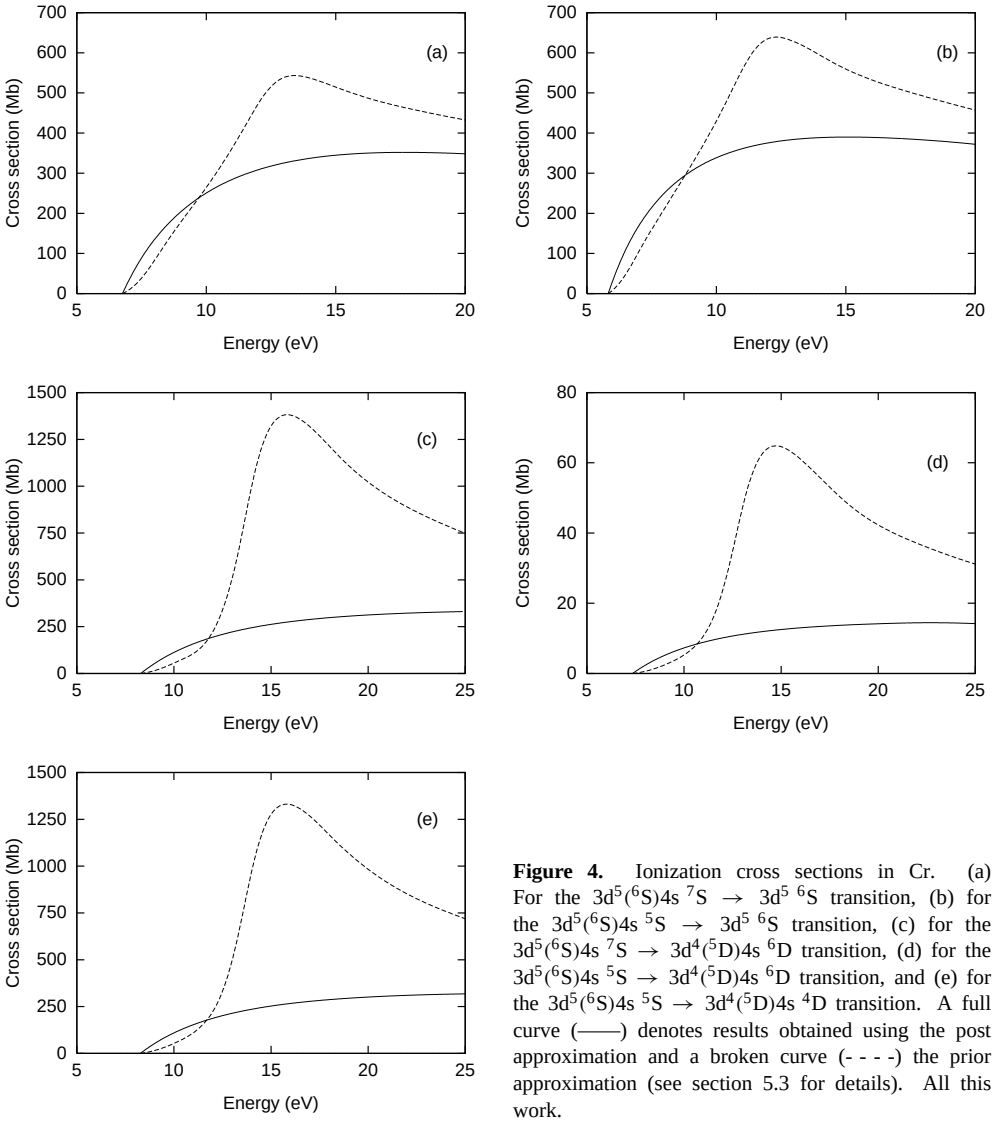

Figure 4. Ionization cross sections in Cr. (a) For the $3d^5(^6S)4s\ ^7S \rightarrow 3d^5\ ^6S$ transition, (b) for the $3d^5(^6S)4s\ ^5S \rightarrow 3d^5\ ^6S$ transition, (c) for the $3d^5(^6S)4s\ ^7S \rightarrow 3d^4(^5D)4s\ ^6D$ transition, (d) for the $3d^5(^6S)4s\ ^5S \rightarrow 3d^4(^5D)4s\ ^6D$ transition, and (e) for the $3d^5(^6S)4s\ ^5S \rightarrow 3d^4(^5D)4s\ ^4D$ transition. A full curve (——) denotes results obtained using the post approximation and a broken curve (- - - -) the prior approximation (see section 5.3 for details). All this work.

5.4. Photon efficiencies—$\mathcal{SXB}$ ratios

We present our results for the $\mathcal{SXB}_{\sigma\rho}$ ratios for Cr and Mo as a function of electron temperature and density in tabular form (tables 3 and 4), for ease of use by plasma modellers, and in graphical form (figures 6 and 7) so as to illustrate best their temperature and density dependence. Behringer *et al* (1989) presented results for $\mathcal{SXB}_{\sigma\sigma}$ ratios for the 4270.7 Å and 5208.3 Å lines in Cr, which were obtained in the low-density limit. Our low-density limit results ($N_e \leqslant 10^{12}$ cm^{-3}) are a factor of 2–3 smaller than those of Behringer *et al* (1989). This is due in the main to their use of the Burgess–Chidichimo (1983) general formula for the ionization rate coefficients as opposed to our *ab initio* calculations. Although there is a strong temperature dependence to the $\mathcal{SXB}$ ratios at divertor temperatures (a few eV) this dependence is not sensitive to the choice of approximation used. The results of Behringer *et al* (1989) exhibit the same (Maxwellian) temperature dependence as ours.

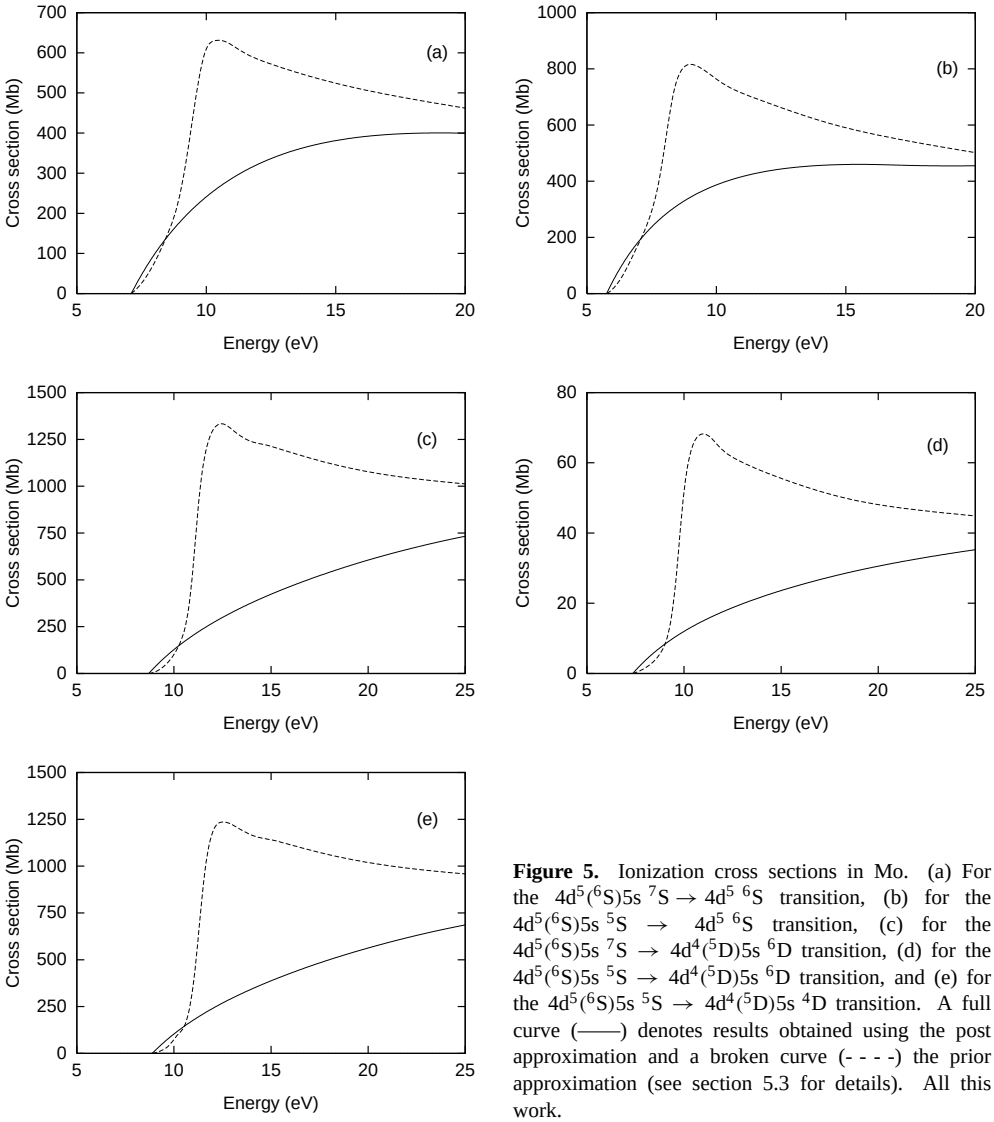

Figure 5. Ionization cross sections in Mo. (a) For the $4d^5(^6S)5s\ ^7S \rightarrow 4d^5\ ^6S$ transition, (b) for the $4d^5(^6S)5s\ ^5S \rightarrow 4d^5\ ^6S$ transition, (c) for the $4d^5(^6S)5s\ ^7S \rightarrow 4d^4(^5D)5s\ ^6D$ transition, (d) for the $4d^5(^6S)5s\ ^5S \rightarrow 4d^4(^5D)5s\ ^6D$ transition, and (e) for the $4d^5(^6S)5s\ ^5S \rightarrow 4d^4(^5D)5s\ ^4D$ transition. A full curve (——) denotes results obtained using the post approximation and a broken curve (- - - -) the prior approximation (see section 5.3 for details). All this work.

5.4.1. Direct $\mathcal{SXB}_{\sigma\sigma}$ ratios. We observe little density dependence below $N_e = 10^{13}$ cm^{-3}, which is the density regime applicable to the edge plasma, see figures 6 and 7. As the electron density increases through 10^{14} cm^{-3}, which is applicable to the divertor region, the $\mathcal{SXB}_{\sigma\sigma}$ ratios show a rapid increase as collisional de-excitation and ionization become competitive with radiative transitions as a mechanism for depopulating the upper states (see equation (A8)). As the electron density increases further through 10^{15} cm^{-3}, radiative depopulation becomes negligible compared to collisional de-excitation and ionization and so collisional equilibrium is reached, and then the $\mathcal{SXB}_{\sigma\sigma}$ ratios exhibit their pure N_e^1 scaling. We note that the dominant density effect is collisional de-excitation, the inverse of our primary excitation transitions, and direct ionization. The effect of other excited states, not included in figure 1, is relatively small, see also Behringer *et al* (1989). We note that the Mo $\mathcal{SXB}_{55}$ ratio for the $y\ ^5P^o \rightarrow a\ ^5S$ line exhibits a different density dependence

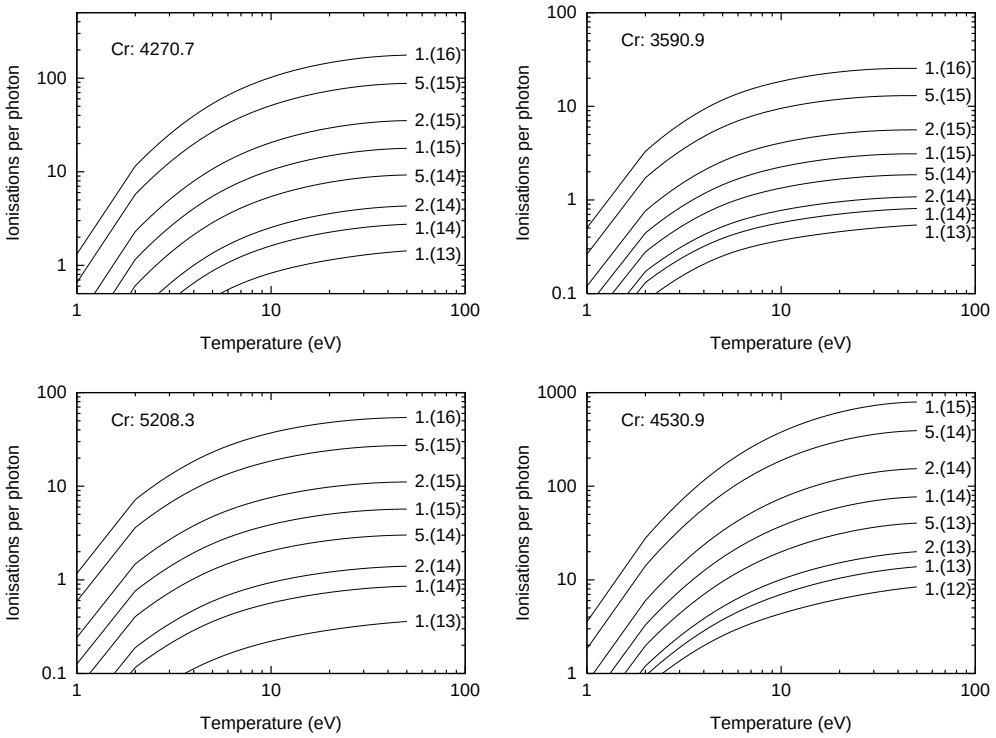

Figure 6. Direct $\mathcal{SXB}_{\sigma\sigma}$ ratios (ionizations per photon) for Cr as a function of electron temperature (eV) and density (cm^{-3}). For $z\ ^7P^o \rightarrow a\ ^7S$ ($\lambda = 4270.7$ Å); $y\ ^7P^o \rightarrow a\ ^7S$ ($\lambda = 3590.9$ Å); $z\ ^5P^o \rightarrow a\ ^5S$ ($\lambda = 5208.3$ Å); $y\ ^5P^o \rightarrow a\ ^5S$ ($\lambda = 4530.9$ Å), line emission. All this work.

from all of the other ratios. As the density increases initially, the de-population of the $y\ ^5P^o$ upper-state, by collisional de-excitation and ionization, is more than outweighed by a net population transfer by collisional excitation from the $z\ ^5P^o$ and so the $\mathcal{SXB}_{55}$ ratio decreases. Eventually, as the density increases further, the depopulating mechanisms dominate and the $\mathcal{SXB}_{55}$ ratio starts to increase. That a similar behaviour is not observed in Cr is simply due to fact that the relative populating and depopulating mechanisms have somewhat different relative strengths and the net transfer from the $z\ ^5P^o$ to the $y\ ^5P^o$ is never competitive with the dominant depopulating mechanisms.

5.4.2. Exchange $\mathcal{SXB}_{\sigma\rho}$ ratios. The exchange $\mathcal{SXB}_{57}$ ratios for the metastable cross-coupling, which can be viewed as a loss from the septet lines or an enhancement of the quintet lines (see equations (2.17)–(2.18)) are given in tabular form only, see tables 3(*e*), (*f*) and 4(*e*), (*f*). The key quantity is the ratio of $\mathcal{SXB}_{55}$ to $\mathcal{SXB}_{57}$ (see equation (2.18)). For the strong $z\ ^5P^o \rightarrow a\ ^5S$ lines this ratio is less than 0.1 for temperatures greater than 2 eV at all densities for both Cr (compare tables 3(*c*) and (*e*)) and Mo (compare tables 4(*c*) and (*e*)). Even down at 1 eV, neglect of metastable cross-coupling only results in an overestimate of the flux by 20% (Cr) or 30% (Mo). At temperatures of less than 1 eV the correction factor due to this ratio becomes more significant but we have set a lower limit of 1 eV on our results since the deduction of impurity flux from observed line emission requires that (virtually) all of the neutrals be ionized (see section 2). For the case of the weak

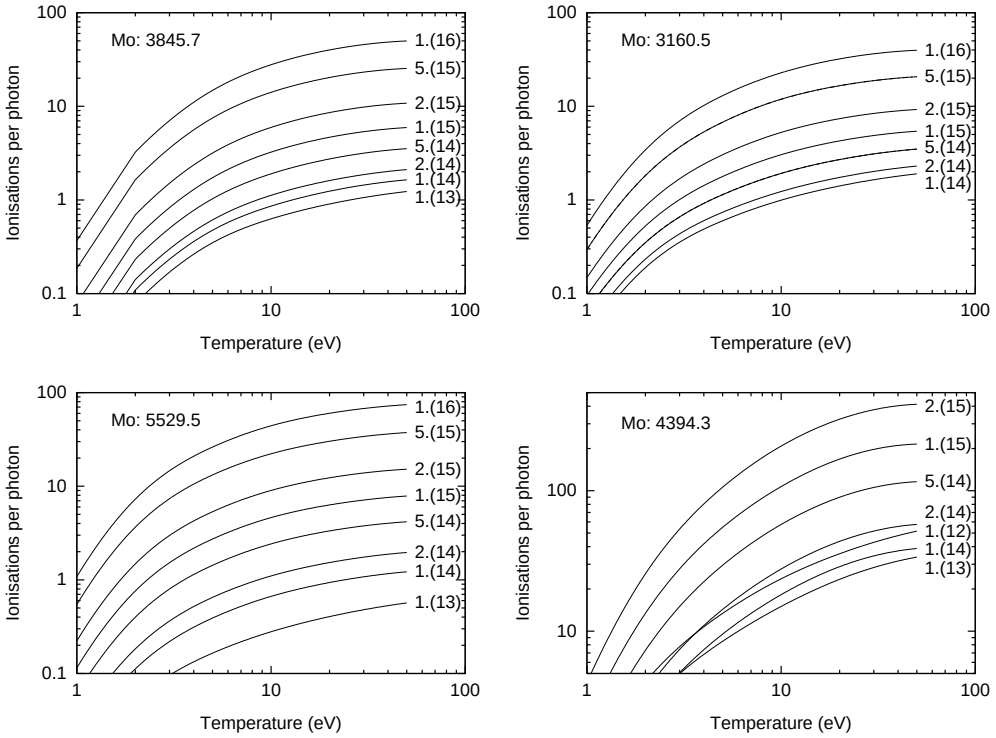

Figure 7. Direct $\mathcal{SXB}_{\sigma\sigma}$ ratios (ionizations per photon) for Mo as a function of electron temperature (eV) and density (cm^{-3}). For $z\ ^7P^o \rightarrow a\ ^7S$ ($\lambda = 3845.7$ Å); $y\ ^7P^o \rightarrow a\ ^7S$ ($\lambda = 3160.5$ Å); $z\ ^5P^o \rightarrow a\ ^5S$ ($\lambda = 5529.5$ Å); $y\ ^5P^o \rightarrow a\ ^5S$ ($\lambda = 4394.3$ Å), line emission. All this work.

$y\ ^5P^o \rightarrow a\ ^5S$ lines the ratio of $\mathcal{SXB}_{55}$ to $\mathcal{SXB}_{57}$ is less than 0.1 only at much higher temperatures (less so at higher densities), compare tables 3(d) and (f) for Cr and tables 4(d) and (f) for Mo, and cannot be neglected if these lines are used. For example, at 1 eV and at low density the ratio is 2.4 and 3.9 for Cr and Mo, respectively.

5.5. Transient ionization

There are two questions that can be addressed by studying the time evolution of the metastable populations and ionization fractions. First, do the metastable populations have time to evolve to their equilibrium values before the atom is ionized, i.e. does the dominant radiation from the neutral atom occur when the metastables are in equilibrium or not? Second, how are the metastables initially distributed as the atoms are sputtered off the surface? To this end we solved for the evolution of the populations using equation (2.10) over $t = 0$ to 10^{-3} s, over the range of temperatures 1–10 eV, for an electron density of 2×10^{13} cm^{-3} for both Cr and Mo. Results for alternative electron densities can be obtained, to a good approximation, by rescaling the time, i.e. by assuming that $N_e t$ is a constant.

5.5.1. Mo. We present our fractional populations for Mo, Mo^+ and Mo^{2+} at $t = 5 \times 10^{-8}, 4 \times 10^{-7}, 4 \times 10^{-6}$ and 1×10^{-4} s in figure 8 for an initial population distributed totally in the ^7S ground term of Mo. We focus on the results at temperatures of 1 and 10 eV

since they illustrate different limiting behaviour. The $T = 1$ eV results are applicable to a divertor plasma (e.g. Mo target-plates) and the $T \geqslant 10$ eV results are applicable to the edge plasma (Cr RF shielding and Mo belt-limiters). For a $T = 10$ eV plasma we find that the ground ^{7}S and metastable ^{5}S term populations do not equilibrate until about $t = 4 \times 10^{-6}$ s, see figure 8. Note the '7/5' population ratio only applies at high temperatures, at $T = 1$ eV the $\exp(\Delta E(^5\mathrm{S} - {}^7\mathrm{S})/kT)$ factor is significantly larger than unity. However, by this time ($t = 4 \times 10^{-6}$ s) we see also that the fractional abundance is dominated by Mo^+ and Mo^{2+}. Note that the Mo^+ populations are metastable-resolved because of our final-state resolved ionization data but the Mo^{2+} populations are not, there is just a total loss to the $+2$ charge state and a single population for it. Thus, for the edge plasma, the radiation emitted from the neutral occurs while the ^{5}S metastable term is *not* in equilibrium with the ^{7}S ground term. If we now focus on the results at $T = 1$ eV we see that Mo is still the dominant ionization stage at $t = 4 \times 10^{-6}$ s (see figure 8) where the ground and metastable terms equilibrate and, indeed, that Mo^+ and Mo^{+2} do not dominate until at least $t = 10^{-4}$ s. Thus, for a divertor plasma, the radiation emitted from the neutral is dominated by far by that emitted when the ^{5}S metastable term *is* in equilibrium with the ^{7}S ground term. Of course if one looks close to the surface where the atom has had insufficient time ($t < 4 \times 10^{-6}$ s) to equilibrate the ground and metastable terms, the radiation is again emitted as in the transient case. We also solved the time-dependent population equations with an initial population distributed totally in the ^{5}S metastable term of Mo. This enabled us to see clearly when the ground and metastable terms had equlibrated—then the populations coincide with those evolved from the previous initial condition. As we observe below in section 5.6, it appears that the experimental situtation favours the initial population being in the ground term and so we do not present any detailed transient ionization results for the initial population being in the metastable term. Finally, the transient behaviour of the heavy metals, namely the metastable versus ionization relaxation times at 'low' and 'high' temperatures, is similar to that found in preliminary studies on light species (Be, C) by Dickson (1993).

5.5.2. Cr. We present our fractional populations for Cr, Cr^+ and Cr^{2+} at $t = 4 \times 10^{-7}$ and 1×10^{-4} s in figure 9 for an initial population distributed totally in the ^{7}S ground term of Cr. This initial $t = 0$ distribution evolves smoothly in time to reach the situation at $t = 4 \times 10^{-7}$ s where the ^{7}S ground term and ^{5}S metastable term have equilibrated. At this time, as with Mo, the dominant ionization stage at $T = 1$ eV is still the neutral while at $T = 10$ eV Cr^+ is the dominant ionization stage. Again Cr^+ does not dominate down at $T = 1$ eV until at least $t = 1 \times 10^{-4}$ s. The difference compared to Mo is that equilibration between the ground and metastable terms of Cr takes place at an earlier time for Cr, after $\sim 4 \times 10^{-7}$ s rather than $\sim 4 \times 10^{-6}$ s (compare figures 8 and 9). This means that the Cr equilibrated population structure is simpler than that for Mo since it has had less time to evolve. We note that the Cr $^7\mathrm{S} \rightarrow {}^5\mathrm{S}$ excitation rate coefficient is a factor of 2–3 larger than that for Mo over $T = 1$–10 eV.

5.6. Connections with observations

The $z\ ^7\mathrm{P^o} \rightarrow a\ ^7\mathrm{S}$, $y\ ^7\mathrm{P^o} \rightarrow a^7\mathrm{S}$ and $z\ ^5\mathrm{P^o} \rightarrow a\ ^5\mathrm{S}$ Mo lines have been observed† in FTU at Frascati (Gatti 1995 private communication) at a temperature of $T \geqslant 10$ eV (the Mo source here is a limiter in the main vessel, not a divertor target). A metastable fraction of about

† The lines actually observed are from levels within the upper term. In appendix B to this paper we show how term-resolved emissivities can be deduced from level-resolved emissivities for use with the $\mathcal{SXB}$ ratios presented here.

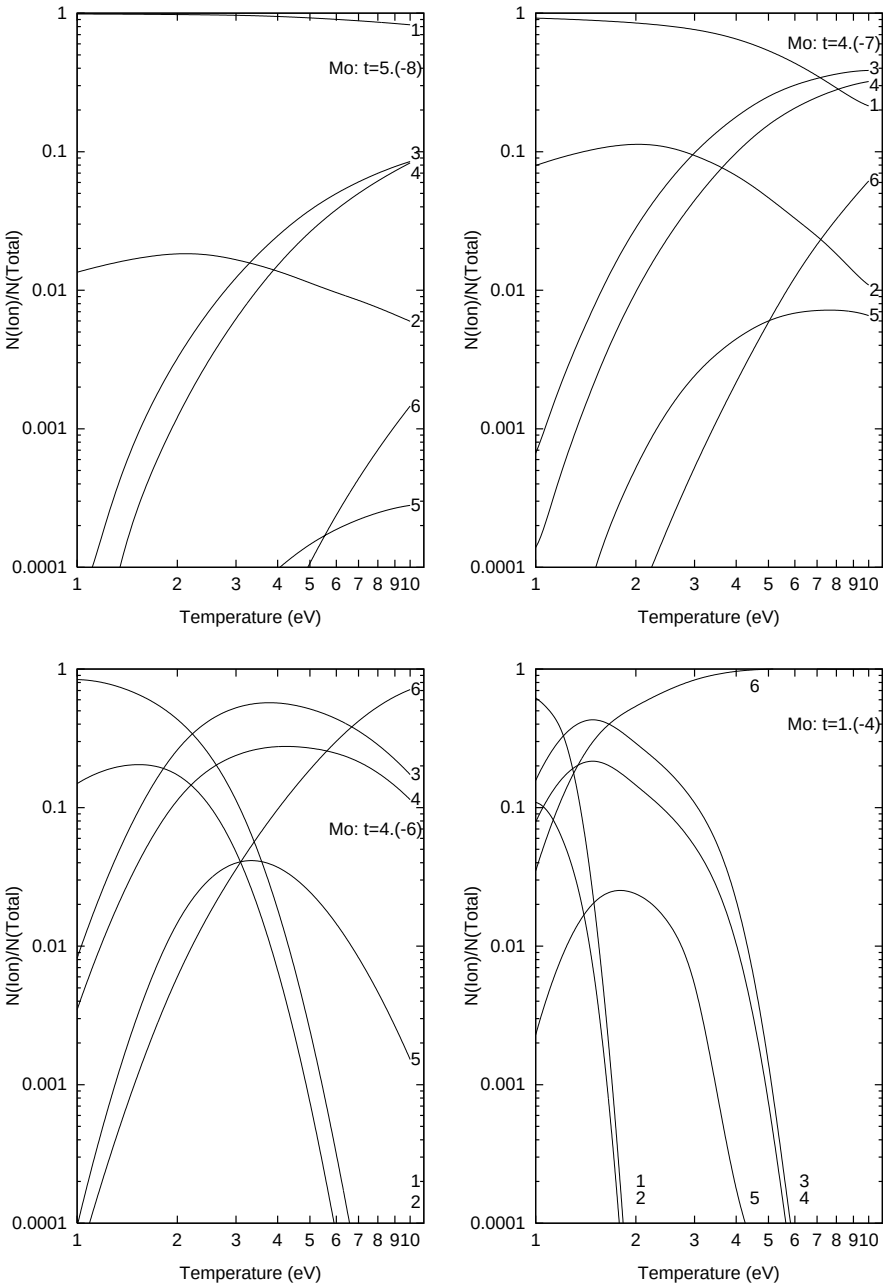

Figure 8. Population fractions for Mo at the times $t = 5\times10^{-8}$ s, $t = 4\times10^{-7}$ s, $t = 4\times10^{-6}$ s and $t = 1\times10^{-4}$ s. Index: 1, Mo ^{7}S; 2, Mo ^{5}S; 3, Mo$^+$ ^{6}S; 4, Mo$^+$ ^{6}D; 5, Mo$^+$ ^{4}D; 6, Mo^{2+} unresolved. All this work.

10% for Mo was determined using the $\mathcal{SXB}_{\sigma\rho}$ ratios that we have presented here. At these high temperatures the metastable is not in collisional equilibrium with the ground term. The 10% metastable fraction is consistent with the atoms sputtering off the surface (with almost all of them) in the ground state, see figure 8. This 10% fraction, combined with an $\mathcal{SXB}_{55}$

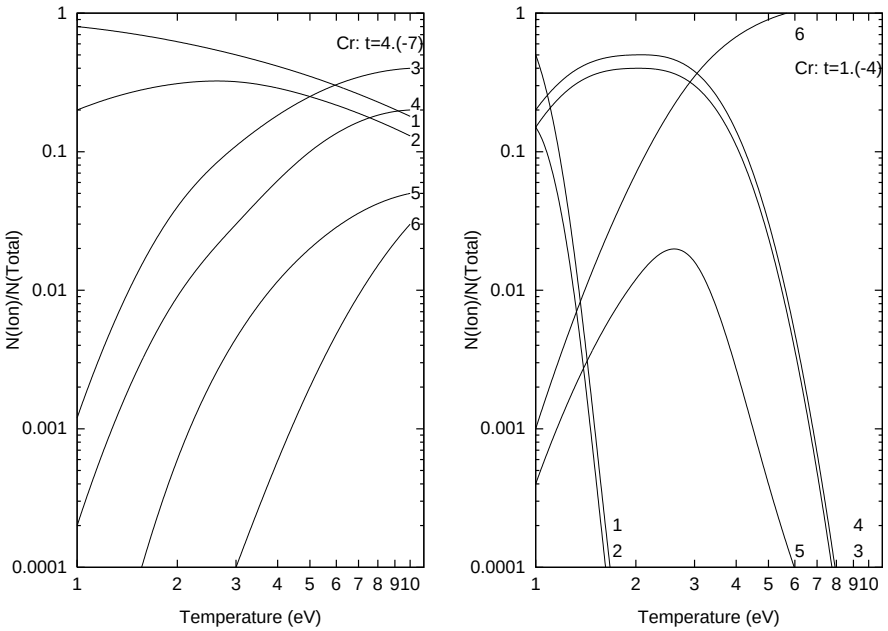

Figure 9. Population fractions for Cr at the times $t = 4 \times 10^{-7}$ s and $t = 1 \times 10^{-4}$ s. Index: 1, Cr ^{7}S; 2, Cr ^{5}S; 3, Cr$^+$ ^{6}S; 4, Cr$^+$ ^{6}D; 5, Cr$^+$ ^{4}D; 6, Cr^{2+} unresolved. All this work.

to $\mathcal{SXB}_{57}$ ratio of about 0.01 (see tables 4(*c*) and (*e*)), means that the emissivity in the $z\ ^5\mathrm{P^o} \rightarrow a^5\mathrm{S}$ metastable line is dominated (90%) by excitation from the ^{5}S metastable term and not from the ^{7}S ground term (see equation (2.24)). Finally, for electron densities found in the divertor region, we emphasize that the $\mathcal{SXB}_{\sigma\rho}$ ratios for Mo are *not* well described by either of the low-density 'coronal approximation' or high-density 'collisional equilibrium' limiting cases. A (metastable-resolved) collisional–radiative description is necessary.

6. Conclusion

We have carried out calculations of energy levels, radiative rates and electron impact excitation and ionization cross sections for Cr and Mo using state-of-the-art atomic physics codes. We have used these atomic data in the generalized collisional–radiative package ADAS to calculate density-dependent $\mathcal{SXB}$ ratios of use for studying impurity influx from the divertor plates (Mo) and RF heating antennae (Cr) of a magnetic fusion tokamak. We found that an explicit density-dependent metastable-resolved collisional–radiative description was necessary at divertor densities and temperatures. We also found that metastable cross-coupling could be neglected for the strong z-lines but not for the weak y-lines in Cr and Mo. Transient ionization was studied and found to be of importance for the edge plasma and for near-surface observations from a divertor plasma. This study demonstrates the feasibility and paves the way for future studies of spectral diagnostics of near-neutral heavy species in cool dense plasmas using techniques that were originally developed and exploited for light species in hot dilute plasmas.

Acknowledgments

We would like to thank the members of the Opacity Project and the Iron Project for the use of their original *R*-matrix codes. We would also like to thank Dr V M Burke for providing us with a copy of the FARM code prior to publication. This work was supported in part by the JET Joint Undertaking, a NATO travel grant CRG 940134 with the University of Strathclyde, and the US Department of Energy, Office of Fusion Energy, under contract No DE-FG05-86-ER53217 with Auburn University.

Appendix A

We remove the restrictions imposed in section 2. We define the collisional–radiative matrix elements

$$C_{ij} = \frac{1}{N_e} A_{j\to i} + q_{j\to i} \qquad \text{for } i \neq j \tag{A1}$$

and

$$C_{ii} = -\sum_{j\neq i} C_{ij} - S_i^{(z\to z+1)}, \tag{A2}$$

which apply both to, and between, metastables and excited states. The excited state populations are now given by

$$N_j^z = -\sum_{\sigma,i} C_{ji}^{-1} C_{i\sigma} N_\sigma^z - \sum_{\mu,i} C_{ji}^{-1} S_{i\mu}^{(z-1\to z)} N_\mu^{z-1} \tag{A3}$$

$$\equiv \sum_\sigma F_{j\sigma}^{X} N_e N_\sigma^z + \sum_\mu F_{j\mu}^{I} N_e N_\mu^{z-1}. \tag{A4}$$

The coefficient $F_{j\sigma}^{X}$ represents the effective contribution to the population of j due to excitation from the metastable σ and $F_{j\mu}^{I}$ the contribution due to ionization from μ. Thus the emissivity in the $i \to j$ transition is given by

$$\varepsilon_{i\to j} = N_e A_{i\to j} \sum_\sigma F_{i\sigma}^{X} N_\sigma^z + N_e A_{i\to j} \sum_\mu F_{i\mu}^{I} N_\mu^{z-1} \tag{A5}$$

$$\equiv \varepsilon_{i\to j}^{X} + \varepsilon_{i\to j}^{I}. \tag{A6}$$

A solution can be obtained for the metastable populations on using a set of linearly independent lines, indexed by ρ, equal to the number of metastables. Then,

$$\varepsilon_\rho \equiv \varepsilon_{\rho,i\to j}^{X} = \sum_\sigma S_{CR,\sigma}^{(z\to z+1)} N_e N_\sigma / \mathcal{SXB}_{\rho\sigma}^z \tag{A7}$$

where

$$\mathcal{SXB}_{\rho\sigma}^z \equiv \frac{S_{CR,\sigma}^{(z\to z+1)}}{A_{i\to j} F_{i\sigma}^{X}} \tag{A8}$$

and

$$S_{CR,\sigma}^{(z\to z+1)} = \sum_\nu S_{CR,\sigma\to\nu}^{(z\to z+1)}, \tag{A9}$$

where

$$S_{CR,\sigma\to\nu}^{(z\to z+1)} = S_{\nu\sigma}^{(z\to z+1)} - \sum_{j,i} C_{\nu j} C_{ji}^{-1} S_{i\nu}^{(z\to z+1)} \tag{A10}$$

is the generalized collisional–radiative ionization rate coefficient from metastable σ of ionization stage Z to metastable ν of the parent stage. Finally, neglecting the ionization contribution to the emissivity, we have that

$$N_{\rm e} N_\sigma^z S_{{\rm CR},\sigma}^{(z\to z+1)} = \sum_\rho (\mathcal{R}^z)_{\sigma\rho}^{-1} \varepsilon_\rho \tag{A11}$$

and so the impurity flux is now given by

$$\Gamma = \sum_{\sigma,\rho} (\mathcal{R}^z)_{\sigma\rho}^{-1} I_\rho, \tag{A12}$$

where we have used the photon efficiency, $\mathcal{R}(= \mathcal{SXB}^{-1})$, instead of the $\mathcal{SXB}$ ratio.

For transient ionization, the metastable populations of stage Z now satisfy

$$\frac{1}{N_{\rm e}} \frac{{\rm d}N_\sigma^z}{{\rm d}t} = \sum_\rho (X_{{\rm CR},\rho\to\sigma}^{(z\to z)} N_\rho^z - X_{{\rm CR},\sigma\to\rho}^{(z\to z)} N_\sigma^z) + \sum_\mu S_{{\rm CR},\mu\to\sigma}^{(z-1\to z)} N_\mu^{z-1} - \sum_\nu S_{{\rm CR},\sigma\to\nu}^{(z\to z+1)} N_\sigma^z, \tag{A13}$$

where

$$X_{{\rm CR},\sigma\to\rho}^{(z\to z)} = C_{\rho\sigma} - \sum_{j,i} C_{\rho j} C_{ji}^{-1} C_{i\sigma} \tag{A14}$$

is the generalized collisional–radiative metastable cross-coupling rate coefficient from metastable σ to metastable ρ of ionization stage Z.

The initial metastable populations (cf section 2.3.1) can be reconstructed using

$$N_\sigma^z(t=0) = \frac{1}{\nu} \sum_\rho (\mathcal{R}^z)_{\sigma\rho}^{-1} I_\rho^z - \frac{1}{\nu} \sum_{\mu,\nu} S_{{\rm CR},\mu\to\sigma}^{(z-1\to z)} (\mathcal{R}^{z-1})_{\mu\nu}^{-1} I_\nu^{z-1} / S_{{\rm CR},\mu}^{(z-1\to z)}. \tag{A15}$$

The energies $\mathcal{W}_{\rm tot}(t)$ and $\mathcal{W}_{\rm tot}^{\rm excess}(t)$, given by equations (2.11) and (2.12), can then be evaluated using the populations determined via equations (A13)–(A14) and a chosen initial distribution, or that determined from (A15). Finally, the line-emission power coefficient is now given by

$$P_{{\rm L},\sigma}^z = \sum_{j,k} \Delta E_{jk} A_{j\to k} F_{j\sigma}^{\rm X}. \tag{A16}$$

Sometimes one deals with the photon-emissivity rate coefficient, $\mathcal{PEC}$, rather than the $\mathcal{SXB}$ ratio. The two are related as follows:

$$\mathcal{PEC}_{\sigma\rho}^{\rm X} \equiv \mathcal{PEC}_{\sigma\rho,i\to j}^{\rm X} = A_{i\to j} F_{i\sigma}^{\rm X} \tag{A17}$$

and then, from equation (A8),

$$\mathcal{SXB}_{\rho\sigma}^z \equiv \frac{S_{{\rm CR},\sigma}^{(z\to z+1)}}{\mathcal{PEC}_{\sigma\rho}^{\rm X}}. \tag{A18}$$

Similarly, one can define ionization (and recombination) $\mathcal{PEC}$s in the obvious way, compare equations (A5), (A6) and (A17), while the $\mathcal{SXB}$ ratio is only meaningful for excitation.

Appendix B

We show how term-resolved emissivities can be determined from (observed) level-resolved emissivities for use with our term-resolved $\mathcal{SXB}$ ratios. The level-resolved emissivities ($J \to J'$) and term-resolved emissivities ($LS \to L'S$) are given by

$$\varepsilon_{J\to J'} = N_J A_{J\to J'} \tag{B1}$$

and

$$\varepsilon_{LS\to L'S} = N_{LS} A_{LS\to L'S} \tag{B2}$$

respectively. Assuming that the upper levels are populated statistically within the term, i.e.

$$N_J = \frac{(2J+1)N_{LS}}{(2S+1)(2L+1)}, \tag{B3}$$

we have that

$$\varepsilon_{J\to J'} = \frac{(2J+1)A_{J\to J'}}{(2S+1)(2L+1)A_{LS\to L'S}}\varepsilon_{LS\to L'S}. \tag{B4}$$

If the required theoretical level-resolved and term-resolved radiative rates are available then term-resolved emissivities can be obtained from level-resolved observed (line-of-sight) emissivities (via equation (B4)) for use with our term-resolved $\mathcal{SXB}$ ratios. The use of equation (B4) allows for (small) departures from LS-coupling. If the appropriate radiative rates are not available then LS-coupling must be assumed. Then for electric 2^k-pole radiation we have that (Cowan 1981)

$$A_{J\to J'} = A_{LS\to L'S}(2L+1)(2J'+1)\begin{Bmatrix} L & J & S \\ J' & L' & k \end{Bmatrix}^2 \tag{B5}$$

where $\{\cdots\}$ denotes the Wigner $6j$-symbol (Edmonds 1957). Using equation (B3) again, we have that

$$\varepsilon_{J\to J'} = \varepsilon_{LS\to L'S}\frac{(2J+1)(2J'+1)}{(2S+1)}\begin{Bmatrix} L & J & S \\ J' & L' & k \end{Bmatrix}^2. \tag{B6}$$

Thus in this case equation (B6) can be used to determine term-resolved emissivities instead of equation (B4).

For Cr/Mo in particular we have ${}^7\mathrm{P}^{\mathrm{o}}_J \to {}^7\mathrm{S}_{J'}$ and ${}^5\mathrm{P}^{\mathrm{o}}_J \to {}^5\mathrm{S}_{J'}$ where $k = 1$, $J' = S = 3$ or 2 and $L' = 0$ and $L = 1$. From Edmonds (1957) we have that

$$\begin{Bmatrix} 1 & J & S \\ S & 0 & 1 \end{Bmatrix}^2 = \frac{1}{3(2S+1)}. \tag{B7}$$

Then from equations (B6) and (B7) we have

$$\varepsilon({}^7\mathrm{P}^{\mathrm{o}} \to {}^7\mathrm{S}) = \frac{21}{(2J+1)}\varepsilon({}^7\mathrm{P}^{\mathrm{o}}_J \to {}^7\mathrm{S}_3), \tag{B8}$$

where $J = 2, 3$ or 4, and

$$\varepsilon({}^5\mathrm{P}^{\mathrm{o}} \to {}^5\mathrm{S}) = \frac{15}{(2J+1)}\varepsilon({}^5\mathrm{P}^{\mathrm{o}}_J \to {}^5\mathrm{S}_2), \tag{B9}$$

where $J = 1, 2$ or 3, depending on the line observed. For these transitions the coefficients in equations (B8) and (B9) are just

$$\frac{(2S+1)(2L+1)}{(2J+1)} \tag{B10}$$

as expected. This follows from the orthogonality relation for a $6j$-symbol and the fact that in this case there is a single final level ($J' = S$).

References

Badnell N R 1984 *J. Phys. B: At. Mol. Phys.* **17** 4013
——1986 *J. Phys. B: At. Mol. Phys.* **19** 3827
——1988 *J. Phys. B: At. Mol. Opt. Phys.* **21** 749
Badnell N R, Dickson W J, Griffin D C, Pindzola M S and Summers H P 1993a *AIP Conf. Proc.* **332** 84
Badnell N R, Pindzola M S, Dickson W J, Summers H P, Griffin D C and Lang J 1993b *Astrophys. J.* **407** L91
Bartschat K 1993 *J. Phys. B: At. Mol. Opt. Phys.* **26** 3595
Bartschat K, Hudson E T, Scott M P, Burke P G and Burke V M 1996 *J. Phys. B: At. Mol. Opt. Phys.* **29** 115
Behringer K, Summers H P, Denne B, Forrest M and Stamp M 1989 *Plasma Phys. Control Fusion* **31** 2059
Berrington K A, Burke P G, Butler K, Seaton M J, Storey P J, Taylor K T and Yu Yan 1987 *J. Phys. B: At. Mol. Phys.* **20** 6379
Berrington K A, Burke P G, Hibbert A, Mohan M and Baluja K L 1988 *J. Phys. B: At. Mol. Opt. Phys.* **21** 339
Berrington K A, Eissner W B and Norrington P H 1995 *Comput. Phys. Commun.* **92** 290
Blackwell D E, Menon S L R and Petford A D 1984 *Mon. Not. R. Astron. Soc.* **207** 535
Botero J and Macek J H 1991 *J. Phys. B: At. Mol. Opt. Phys.* **24** L405
Burgess A and Chidichimo M C 1983 *Mon. Not. R. Astron. Soc.* **203** 1269
Burgess A, Hummer D G and Tully J A 1970 *Phil. Trans. R. Soc.* **266** 225
Burgess A and Tully J A 1978 *J. Phys. B: At. Mol. Phys.* **11** 4271
——1992 *Astron. Astrophys.* **254** 436
Burke P G and Berrington K A 1993 *Atomic and Molecular Processes—An R-matrix Approach* (Bristol: IOP)
Burke P G, Berrington K A and Sukumar C V 1981 *J. Phys. B: At. Mol. Phys.* **14** 289
Burke P G, Burke V M and Dunseath K M 1994 *J. Phys. B: At. Mol. Opt. Phys.* **27** 5341
Burke P G, Kingston A E and Tait J H 1989 *Atomic Data for Spectroscopic Studies on JET* (JET Order No: JT8/12784)
Burke P G and Taylor A J 1966 *Proc. Phys. Soc.* **88** 549
Burke V M, Burke P G and Scott N S 1992 *Comput. Phys. Commun.* **69** 76
Burke V M and Noble C J 1995 *Comput. Phys. Commun.* **85** 471
Cowan R D 1981 *The Theory of Atomic Structure and Spectra* (Berkeley, CA: University of California Press)
Croskery J P, Scott N S, Bell K L and Berrington K A 1982 *Comput. Phys. Commun.* **27** 385
Dickson W J 1993 *Ph.D. Dissertation* University of Strathclyde
Edmunds A R 1957 *Angular Momentum in Quantum Mechanics* (Princeton, NJ: Princeton University Press)
Eissner W, Jones M and Nussbaumer H 1974 *Comput. Phys. Commun.* **8** 270
Freund R S, Wetzel R C, Shul R J and Hayes T R 1990 *Phys. Rev.* A **41** 3575
Froese Fischer C 1991 *Comput. Phys. Commun.* **64** 369
Gorczyca T W, Pindzola M S, Badnell N R and Griffin D C 1994 *Phys. Rev.* A **49** 4682
Gorczyca T W, Robicheaux F, Pindzola M S, Griffin D C and Badnell N R 1995 *Phys. Rev.* A **52** 3877
Griffin D C and Pindzola M S 1995 *J. Phys. B: At. Mol. Opt. Phys.* **28** 4347
Hibbert A 1989 *Phys. Scr.* **39** 574
Hibbert A, Tait J H, Summers H P and Burke P G 1988 *Nucl. Instrum. Methods* B **31** 276
Huber M C E and Sanderman R J 1977 *Proc. R. Soc.* A **357** 355
Hummer D G, Berrington K A, Eissner W, Pradhan A K, Saraph H E and Tully J A 1993 *Astron. Astrophys.* **279** 298
Jakubowicz H and Moores D L 1981 *J. Phys. B: At. Mol. Phys.* **14** 3733
Macek J H and Botero J 1992 *Phys. Rev.* A **45** R8
Moore C E 1971 *NSRDS-NBS* **35** vols 1–3
Nussbaumer H and Storey P J 1978 *Astron. Astrophys.* **64** 139
Ochkur V I 1964 *Sov. Phys.–JETP* **47** 1766
Pan C and Kelly H P 1990 *Phys. Rev.* A **41** 3624
Percival I C and Seaton M J 1957 *Proc. Camb. Phil. Soc.* **53** 654
Pindzola M S, Griffin D C and Bottcher C 1986 *NATO ASI Series* B **145** 75
Pindzola M S, Griffin D C and Macek J H 1995 *Phys. Rev.* A **51** 2186
Pindzola M S and Robicheaux F 1996 *Phys. Rev.* A submitted
Pindzola M S and Schultz D R 1996 *Phys. Rev.* A **53** 1525
Reid R H G, Bartschat K and Burke P G 1992 *J. Phys. B: At. Mol. Opt. Phys.* **25** 3175
Saraph H E 1972 *Comput. Phys. Commun.* **3** 256
Scholtz T T 1991 *J. Phys. B: At. Mol. Opt. Phys.* **24** 2127
Scott N S and Hibbert A 1982 *Comput. Phys. Commun.* **28** 189

Scott N S and Taylor K T 1982 *J. Phys. B: At. Mol. Phys.* **21** 749
Sheffield J 1994 *Rev. Mod. Phys.* **66** 1015
Stangeby P C and McCracken G M 1990 *Nucl. Fusion* **30** 1225
Summers H P 1994 *Atomic Data and Analysis Structure* JET Joint Undertaking Report JET-IR(94)06
Summers H P and Hooper M B 1983 *Plasma Phys.* **25** 1311
Summers H P and McWhirter R W P 1979 *J. Phys. B: At. Mol. Phys.* **12** 2387
Wesson J A 1987 *Tokamaks* (Oxford: Oxford University Press)
Younger S M 1980 *Phys. Rev.* A **22** 111